AN ABSTRACT OF THE THESIS OF

Bridget M. Hass for the degree of Master of Science in Ocean, Earth, and Atmospheric Sciences presented on May 8, 2015.

Title: Heat Flow along the Southern Costa Rica Margin: Insights on the Updip Limit of Seismicity.

Abstract approved: _____

Robert N. Harris

Heat flow analysis of the Costa Rica convergent margin is carried out for seven core sites drilled during Integrated Ocean Drilling Program (IODP) Expeditions 334 and 344 as part of the Costa Rica Seismogenesis Project (CRISP). These expeditions were designed to develop a better understanding of erosional subduction zones. Heat flow measurements were made to improve estimates of the thermal structure and fluid-flow system of this erosive margin. Drilling sites are located on the incoming plate, and the toe, lower, middle, and upper slopes of the margin. Heat flow estimates for each site are determined according to Bullard analysis using thermal conductivity values measured on board the ship and temperature measurements made in situ. Heat flow values are corrected for effects of seafloor bathymetry and sedimentation. Bathymetry corrections are relatively small, < ±6% for all sites. Sedimentation corrections range from 5-10% at the frontal prism and oceanic plate sites and increase to 10-30% at the middle and upper slope sites where rapid sedimentation rates suppresses heat flow. Heat flow on the incoming plate is approximately 160 to 210 mW/m^2, decreases to 116 mW/m^2 on the lower slope and then to values of 46-56 mW/m^2 on the middle and upper slopes. These values agree with previously reported BSR-derived and shallow marine probe measurements and together show a landward

decrease in heat flow consistent with the downward advection of the Cocos plate. Thermal models of the shallow subduction zone successfully predict observed values of heat flow and suggest that temperatures on the subduction thrust increase from 2° C at the deformation front to 100° C at a distance of 45 km landward of the deformation front. The updip limit of seismicity, as defined by aftershocks events of M_L 1-4 recorded following the 1999 M_w 6.9 Quepos earthquake and 2002 M_w 6.4 Osa Earthquake, occurs at cooler temperatures than the 100-150°C typically predicted. I propose that the rough incoming bathymetry of the Cocos Ridge in this sediment-deprived margin enables rupture closer to the surface than at margins with a smooth, heavily sedimented incoming plate.

Heat Flow along the Southern Costa Rica Margin: Insights on the Updip Limit of Seismicity

by
Bridget M. Hass

A THESIS

submitted to

Oregon State University

in partial fulfillment of
the requirements for the
degree of

Master of Science

Presented May 8, 2015
Commencement June 2015

Master of Science thesis of Bridget M. Hass presented on May 8, 2015

APPROVED:

Major Professor, representing Ocean, Earth, and Atmospheric Sciences

Dean of the College of Earth, Ocean, and Atmospheric Sciences

Dean of the Graduate School

I understand that my thesis will become part of the permanent collection of Oregon State University libraries. My signature below authorizes release of my thesis to any reader upon request.

Bridget M. Hass, Author

ACKNOWLEDGEMENTS

This thesis would not have been possible without the help of an amazing support group including faculty at OSU, fellow students, and my amazing friends and family. I would first like to express sincere appreciation to my advisor, Rob Harris, who has been a tremendous support and inspiration throughout my time at OSU as a teacher and mentor. Rob has gone out of his way to provide opportunities for me and has taught me so much in the time I have worked with him. I would also like to thank Michael Hutnak, who I worked for on several heat-flow cruises during my time here. Both Mike and Rob have been incredible mentors, both professionally and personally, and I feel so fortunate to have had the opportunity to work with them. I also could not have started at OSU without the support of Anne Trehu, who advised me my first year and who gave me the opportunity to work on two OBS cruises offshore Chile and Cascadia. Robert Allan has been an incredible help throughout my time here – helping secure funding, providing me guidance, and getting me through stumbling blocks along the way.

I would like to thank fellow geophysics students Patrick Monigle, Jeff Beeson, and Paria Ghorbani, who have been incredible peers and friends. Thank you to my friends who have adventured with me here – I can't list you all but I will cherish memories of mountain biking, climbing, surfing, and exploring the Northwest. Lastly, I want to acknowledge the support of my family: my sisters Carolan and Tacy and parents Robert and Dianne have always been there for me and have been continuous inspirations in my life. I am ever grateful to my grandparents Bob and Lally Hass who have helped shape me in so many ways.

TABLE OF CONTENTS

LIST OF FIGURES

LIST OF TABLES

1 Introduction

Subduction zones are sites of the world's largest earthquakes, yet much is still unknown about the nature of seismogenesis in these tectonic settings. Specifically, there is no clear consensus on the nature of the subduction thrust or the mechanisms controlling the limits and extent of the seismogenic zone. Earthquakes nucleating close to the trench may generate tsunamis as was tragically demonstrated by the 2011 Mw 9.0 Tohoku-Oki and the 2004 Mw 9.2 Sumatra Andaman earthquakes. Conversely, earthquakes that rupture deeper along the thrust often underlie coastal cities and can generate intense generate ground shaking with devastating effects on infrastructure. Temperature is thought to be a key parameter influencing the location and extent of rupture along the subducting plates. The updip limit of seismicity appears to correspond to thrust temperatures of 100-150°C and the downdip limit occurs where the thrust reaches 350-450°C, or the intersection of the subducting plate with the Moho if that occurs at a shallower depth [*Hyndman et al., 1997, Oleskevich et al., 1999*]. This correlation between temperature and the updip position of the seismogenic zone along the subduction thrust has been best demonstrated at accretionary margins [*Hyndman and Wang*, 1993; Oleskevich *et al.*, 1999]. Here I test this correlation at the Costa Rica margin, an erosional subduction zone.

Convergent margins have been broadly categorized into erosional or accretionary end-members [*von Huene and Scholl*, 1991; *Clift and Vannucchi*, 2004]. These end-member models differ primarily in the nature of material transfer between the overriding and downgoing plates. In accretionary margins, material is transferred from the subducting to the overriding plate via frontal thrusting or basal underplating, forming an accretionary prism. In this process the subduction thrust cuts down through the sedimentary section and the plate interface lies within the sediments. Accretion typically occurs in settings where the plate convergence rate is < 6 cm/yr and the sediment thickness is >1 km [*Clift and Vannuchi*, 2004]. In erosive margins, all of the incoming sediment is subducted. The upper surface of the margin subsides and retreats due to basal erosion as the subduction thrust cuts up into the upper plate. If the upper plate has a different lithology than the incoming sediments, then the plate interface of erosive margins may have different frictional conditions than the plate interface of accretionary margins. Subduction

erosion is correlated with settings where plate convergence rates exceed 7.6 cm/yr and the incoming sediment thickness is less than 1 km [*Clift and Vannuchi*, 2004]. Subduction erosion may result from subduction of high-relief topography, such as seamounts, fracture zones, rises, or plate-bending related fractures, which rasp away part of the upper plate.

Offshore Costa Rica (Figure 1) is an ideal location to study the correlation between the updip limit of seismicity and temperature at an erosive margin. Seismicity at this margin is characterized by relatively frequent Mw 6-7 earthquakes with recurrence intervals of ~40 to 50 years [*Protti et al.,* 1994]. An abundance of marine heat flow data has been collected along this margin over the past several decades, allowing for well-constrained thermal models [*Harris et al.,* 2010a,b]. Rapid erosion rates have been inferred along the entire Middle America Trench from subsidence of the continental crust and trench retreat [*Vannucchi et al.*, 2001, 2003]. Erosion is particularly high in the CRISP study area (Figure 1b), the focus of this paper, likely due to the subduction of the overthickened, buoyant Cocos Ridge. Along the CRISP transect, rates of rock removal are estimated to be as high as 1690 km^3/My/km of trench for the past 0.3 My [*Vannucchi et al.,* 2013], which is over an order of magnitude higher than short term erosion rates estimated at Nicoya Peninsula (107-123 km^3/My/km) [*Vannuchi et al.,* 2003].

The most comprehensive study of the thermal regime of this margin was reported by *Harris et al.* [2010a]. This study analyzed heat flow values along 16 trench-perpendicular transects from the Nicoya Peninsula to just northwest of the Osa Peninsula. Heat flow values for that study were determined from shallow marine probe data which measured temperatures 3-4 m below the seafloor, as well as from depths to the temperature-dependent bottom simulating reflectors in seismic reflection sections. Although these techniques allowed for estimates of heat flow over a large spatial extent, they are subject to several shortcomings. Shallow probe temperatures are susceptible to environmental noise such as variations in bottom water temperature, a signal that is greatest near the surface and attenuates with depth. Heat flow estimates from bottom simulating reflectors are subject to picking errors and are based on a number of assumptions including the composition of gas. Temperature data from drilling overcomes these potential deficiencies by providing direct measurements of temperature and thermal conductivity that extend deeper into the subbottom, where surface-related environmental effects are more attenuated.

Harris et al. [2010b] developed finite-element thermal models to fit the heat flow data, with a principal goal of estimating temperatures of the updip limit of seismicity. At the time of that study there was no consistent set of earthquake hypocenters and plate boundary at depth; instead hypocenters of the 1999 Mw 6.9 Quepos earthquake relocated by *DeShon et al.* [2003] were matched with the plate model of *Ranero et al.* [2005]. *Harris et al.* [2010b] found that hydrothermal circulation within the subducting plate was required to fit the heat flow data and emphasized the importance of the thermal structure of the incoming plate.

This study builds on the heat flow data and thermal models developed by *Harris et al.* [2010a,b] in several ways: 1) I incorporate new thermal measurements from the 2011-2012 IODP CRISP Expeditions 334 and 344 [*Vannuchi et al.*, 2012, *Harris et al.*, 2013]. Temperature measurements from drill sites are much deeper than shallow probe measurements, further from near-surface temperature perturbations. These measurements also extend further landward and seaward than do the geothermal probe or BSR-determined heat flow values. 2) A detailed sedimentation history derived from returned cores is used to make sedimentation corrections that yield a more complete estimates of heat flow. The incoming sediment thickness of 100 m determined from drilling at site U1381 is used instead of the 350 m used by *Harris et al*. [2010b]. 3) The model incorporates a new plate geometry consistent with hypocenter locations of aftershocks of $1<M_L<4$ recorded by the CRSEIZE survey in the two months following the 1999 Mw 6.9 Quepos earthquake [*Kyriakopoulos et al.,* in press]. 4) Lastly, I more fully explore the sensitivity of surface heat flow to different permeability structures within the oceanic crust and to the coefficient of friction along the plate boundary.

2 Background

2.1 Tectonic Setting

The Middle America margin is formed by the subduction of the Cocos Plate beneath the Caribbean plate (Figure 1). The margin exhibits along-strike variability in plate convergence rate and obliquity, age and origin of the incoming oceanic plate, morphology, and slab dip. Convergence is nearly orthogonal to the trench and relatively rapid at ~97 mm/yr *DeMets et al*.,

2001]. In the region of the CRISP drilling transect, the incoming oceanic plate was formed at the Cocos-Nazca spreading center (CNS), an intermediate-rate spreading center, and has a crustal age of ~ 16 Ma [*Barckhausen et al.*, 2001]. The incoming oceanic crust is overthickened due to Galapagos hotspot volcanism that formed the aseismic Cocos Ridge, and seamounts making up the ridge result in variable but high-relief. *Walther* [2003] estimates that the Cocos Ridge is elevated on average ~2.5 km higher than the surrounding seafloor, and the oceanic crust has a maximum thickness of ~25 km, up to three times thicker than the normal oceanic crust. The incoming sediment thickness offshore the CRISP transect is ~ 100 m, as determined by drilling at site U1381 [*Vannuchi et al.* 2012, *Harris et al*. 2013].

Seismicity at the CRISP transect was recently summarized by *Arroyo et al.* [2014]. Two recent earthquakes have occurred in the central-southern portion of the Costa Rica margin, the 1999 Mw 6.9 Quepos earthquake and the 2002 Mw 6.4 Osa earthquake. Relocations of the 2002 Osa earthquake indicate that the main shock occurred ~25 km landward from the trench along the plate interface at 5-10 km depth in the vicinity of CRISP IODP site U1379. The authors postulate that underthrusting of the young, buoyant Cocos Ridge has created conditions for seismicity that are shallower and closer to the trench than along other portions of the central Costa Rica margin.

2.2 Overview of Drilling Sites and Lithology

During IODP Expeditions 334 [*Vannuchi et al.,* 2012] and 344 [*Harris et al.,* 2013], four sites were drilled along seismic line BGR99-7 [*Ranero et al.* 2008], herein after referred to as the CRISP transect, and two sites were drilled within the 3D seismic volume [*Bangs et al.,* 2014] NW of the CRISP transect (Figure 1b,c). Lithostratigraphic units at each drill site are summarized briefly below and shown in Figure 2.

Sites U1381 and U1414 are located on the incoming oceanic plate and were drilled in order to characterize material entering the subduction zone. Site U1381 is located on a local basement high. Drilling recovered 95 m of sediment, consisting of two units: a 55 m thick hemipelagic siliceous ooze, Pleistocene in age (<1.89 Ma) overlying a 45 m pelagic calcareous ooze dated to the mid-Miocene. Site U1381 is missing the Pleistocene-mid-Miocene section, indicated by a 9-

11 Ma hiatus in the sediment record. Seventy meters of pillow-basalt basement were recovered during Expedition 334.

Site U1414 is located on the incoming plate within the 3-D seismic volume. This site was drilled to 472 m; 375 m of sediment cover was recovered and 96 m of igneous basement basalt. Three main units were recovered from the slope sediment include 145 m upper unit of silty clay and sand to calcareous nanofossil-rich clay; a 164 m thick middle unit of nannofossil calcareous and silicious ooze with sponge spicules, and a 66 m bottom unit of calcareous and siliceous cemented silt and sandstone.

Sites U1378 and U1380 are located ~15 km landward of the deformation front on the middle slope at 525 and 500 m depth, respectively. These sites are < 1 km apart from one another, and are analyzed together in this study. Drilling at site U1378 recovered the upper 524 m of sediment, and drilling at site U1380 recovered the deeper section. During Expedition 334, site U1380 was drilled to ~480 m, but poor drilling conditions prevented further penetration. The site was revisited during Expedition 344, where drilling extended to 800 meters below sea floor (mbsf). The uppermost unit of the middle slope consists of 128 m of fine, soft, silty-clay sediment with fining upward sandy sequences. Units below consist of layered sedimentary sequences of varying grain size and degrees of lithification, with interspersed clay(stone), silt(stone), and sand(stone).

Sites U1379 and U1413 are located on the upper slope. Site U1379 is ~26 km landward of the trench, and 34 km offshore the Osa Peninsula. U1379 was drilled to ~950 mbsf, and sedimentary units are subdivided into 4 lithostratigraphic units of layered sand and clay(stone), silt(stone) and sand(stone). The basement contact was expected at ~890 m according to reflectors in the seismic line, but during drilling basement was not directly exposed but marked by the first appearance of basalt clasts at 882 m. The lowermost unit is described as a poorly sorted matrix-supported breccia with clasts of limestone, basalt, and mudstone. Site U1413 is located within the 3D seismic volume. Three stratigraphic units of increasingly lithified clay/silt/sand were identified at this site.

3 Thermal Data and Heat Flow Calculations

If thermal physical rock properties are constant and there are no heat sources or sinks, the vertical component of heat flow, q, can be calculated as the product of thermal conductivity, λ, and the temperature gradient dT/dz,

$$q = -\lambda \frac{\partial T}{\partial z} \tag{1}$$

In the presence of varying thermal conductivity, this equation can be rearranged to estimate the background heat flow. In this method, temperatures are expressed as a function of summed thermal resistance, [*Bullard*, 1939],

$$T(z) = T_0 + q \sum_{i=1}^{N} \frac{\Delta z_i}{\lambda(z)_i} \tag{2}$$

where $\lambda(z)_i$ is the thermal conductivity measured over the ith depth interval, dz_i, and the summation is performed over N depth intervals from the surface to the depth of interest z. In practice q and T_0 are estimated by plotting T(z) against summed thermal resistance $\sum_{i=1}^{N} \frac{\Delta z_i}{\lambda(z)_i}$. The best fitting slope of this line yields heat flow.

3.1 Thermal Conductivity

Thermal conductivity is a fundamental thermophysical rock property that affects the thermal structure of the margin. It is a measurement of how easily heat diffuses through a material, and varies with composition and porosity.

Thermal conductivity was measured on recovered cores onboard the ship using full-space needle-probe techniques [*Von Herzen and Maxwell,* 1959] in the upper portions of cores where sediments are unlithified, and half-space line-source techniques [*Vacquier,* 1985] in deeper, more-lithified section of cores. Both of these methods approximate the heating element as an

infinite line source and yield a scalar value of thermal conductivity. These methods are described in detail in the IODP proceedings for each expedition [*Vannuchi et al.*, 2012*; Harris et al.,* 2013], and are outlined briefly below. Full-space measurements are made on whole cores recovered on board the ship using a full-space needle-probe, which contains a thermistor and heating wire. The probe is inserted into a ~2 mm hole in the core liner and temperature is monitored to ensure the core has equilibrated to ambient laboratory temperature, indicated by a background thermal drift of <0.04 mK/min. A calibrated heat pulse is applied, and thermal conductivity values are determined from the observed rise in temperature for the given quantity of heat applied.

Half-space thermal conductivity measurements are made on sediment that is too stiff for the full-space needle to penetrate the core sample without damage. For these basement samples, the needle is exposed on the underside of an epoxy disk and laid against the face of a split core. The surface of the split core must be smooth to ensure sufficient contact with the heating needle. Basement samples are saturated with seawater and equilibrated to room temperature for at least four hours prior to the measurement. During the measurement both the sensor and the sample are insulated to reduce the thermal effects of temperature perturbations within the laboratory. As with the full-space technique, heat is applied through the needle and the observed rise in temperature yields the scalar value of thermal conductivity. Reported full-space values are the average of >3 repeated measurements, and half-space measurements represent the average of 5-10 measurements. The sample re-equilibrated to background temperature for 5-10 minutes between each measurement. Individual measurements are typically within 1% of the mean for both measurement types, and values have <5% uncertainty.

Thermal conductivity values are corrected from laboratory conditions to in situ pressure and temperature assuming a hydrostatic pressure gradient and background temperature gradient obtained from the APCT-3 tool. The pressure correction applied was +1% per 1800 m [*Ratcliffe*, 1960]. Temperature has competing effects on thermal conductivity in porous rocks. Although the thermal conductivity of the rock matrix is inversely related to temperature, the thermal conductivity of water increases with temperature. The temperature correction applied is +1% per +20° C change in temperature between laboratory and in-situ conditions, where temperature is determined from equilibrium measurements described in the following section.

Thermal conductivity measurements for each site are plotted as function of depth and shown with the major lithostratigraphic units (Figure 2). Thermal conductivity for all sites varies from ~0.8 W/m/K near the seafloor to ~1.5 W/m/K at depth. The oceanic plate site U1381 and the margin toe site (U1412) show relatively constant thermal conductivity in the sediment, with values between 0.8-0.9 W/m/K. Thermal conductivity at Site U1414 is also relatively constant through the upper silty clay unit but fluctuates through the sandstone layer. This variability is attributed to a gas disturbance in the core [*Harris et al*., 2013]. Thermal conductivity at site U1412 decreases slightly throughout the uppermost 200m of sediment. At the middle and upper slope sites (U1378, U1380, U1379, U1413), thermal conductivity increases with depth as porosity decreases.

Figure 3 illustrates this relationship between thermal conductivity, lithology, and porosity. Thermal conductivity generally increases with decreasing porosity because sediment grains have a higher thermal conductivity than the water filling the pore spaces. This figure also shows a more subtle correlation between lithology and thermal conductivity. In general sandstone, with greater quartz content, exhibits the highest thermal conductivity while silty clays and calcareous oozes, with higher proportions of clays and organics, have the lowest thermal conductivities.

3.2 Temperature Measurements

The majority of downhole equilibrium temperatures on both expeditions were measured with the Advanced Piston Coring Temperature Tool (APCT-3) [*Heesemann et al*., 2007]. Temperature measurements start by holding the APCT-3, located in the inner core barrel of the piston core cutting shoe, steady at the mudline for 5-10 minutes so that the tool equilibrates with bottom water temperature. The piston core is then lowered to the bottom of the hole and hydraulically shot 9.5 m into undisturbed sediment. This distance is deep enough to avoid thermal perturbations due to drilling. As the APCT-3 is shot into the sediment, heat from the friction of penetration generates a rise in temperature that then decays over a period of 5-10 minutes. Temperature is sampled every second and the temperature-time series is recorded on a microprocessor over a period of at least seven minutes, long enough to extrapolate to equilibrium conditions. The piston core is returned to the surface and the tool is recovered. Formation

equilibrium temperatures are determined by fitting the decay curve using the program TP-Fit [*Heesemann et al*., 2007].

During Expedition 334, the Sediment Temperature (SET) tool [*Davis et al.*, 1997] was used for temperature measurements at site U1381. The tool is deployed on a wireline using a Colleted Delivery System (CDS) and requires a separate wire line trip through the drill pipe. At the bottom of the drill string, the SET tool latches into the Bottom-Hole Assembly (BHA), and extends 4.4 m beyond the bit. As the drill string is lowered, the SET retracts 3.3 m into the BHA and the probe penetrates the formation. Temperatures are typically recorded for 10 minutes, after which the tool is retrieved and data is downloaded on board. Equilibrium temperatures are determined using the TP-fit program.

Thirty in-situ temperature measurements were made at six different sites on Expeditions 334 and 344 (Figure 4, Table 1). With the exception of two temperature measurements made at site U1413 that were discarded due to tool calibration problems, all temperature measurements were deemed high-quality. Most thermal gradients are based on 4-5 equilibrium temperatures measurements. Site U1413 has the least with three and Site U1381 has the most with a total of eight measurements made on both expeditions. The deepest equilibrium temperatures for each site ranged from 63 m at upper slope site U1413 to 110 m at middle slope site U1378, with most measurements ending at depths between 70 and 90 m. All temperature-depth profiles exhibited an approximately linear profile, suggesting heat transfer through the sediment is primarily conductive.

3.3 Heat Flow Determinations

Heat flow was calculated using the Bullard method (Equation 2) for all sites using a least squares fit to the cumulative thermal resistance-temperature plot (Figure 4a). With the exception of Site U1381, residuals are generally small with a mean of 0.2° C (Figure 4b). Site U1381 has anomalously large residuals, with a mean of 0.5° C. The residual plot for this site shows a small offset between measurements made with SET during Expedition 334 and those made with the APCT-3 during Expedition 344. The heat flow and bottom water temperature determined from the SET tool measurements is greater than those determined from the APCT-3 measurements.

Error uncertainties were estimated from the error of the slope to the best fit line to [*Bevington and Robinson*, 2003]. Heat flow values and estimated uncertainties for each site are summarized in Table 1. Heat flow decreases from approximately 190 mW/m^2 on the oceanic plate (Site U1381) to approximately 40 mW/m^2 on the upper slope (Site U1379).

3.4 Environmental Corrections to Heat Flow Data

Before heat flow measurements can be properly interpreted they should be corrected for environmental perturbations. At the Costa Rica margin, these perturbations include distortions to the thermal gradient due bathymetry [*e.g., Blackwell et al.* 1980; *Turcotte and Schubert,* 1982; *Powell et al.* 1988] and the transient cooling effect of sedimentation [*e.g., Powell et al.* 1988*, Hutnak and Fisher*, 2007]. In shallow water, seasonal variations in bottom water temperature can be significant [e.g., *Harris et al.*, 2010a] but at the depth of the IODP temperature measurements are likely attenuated to negligible perturbations.

3.4.1 Bathymetric Corrections

Uneven seafloor bathymetry can distort the near-surface thermal field by compressing isotherms under bathymetric lows, and stretching isotherms under bathymetric highs (Figure 5). This figure shows that a thermal gradient measured on a local ridge will be lower than the background gradient, while a thermal gradient collected in the valley will be higher than the background gradient. The temperature perturbation due to bathymetry is related to the amplitude and wavelength of the topography, and magnitude of the water temperature gradient. For a 2-D sinusoidal surface with amplitude h_0, wavelength L, thermal conductivity, λ, and linear water temperature gradient β, and basal heat flow q_b, the temperature distribution is approximated by,

$$T(x,z) = T_0 + \frac{q_b}{\lambda} z + (\beta - \frac{q_b}{\lambda}) h_0 \cos\left(\frac{2\pi x}{L}\right) e^{-\frac{2\pi z}{L}} \tag{3}$$

[e.g., *Turcotte and Schubert*, 1982]. The temperature disturbance due to bathymetry is given my the right-most term in the equation, and shows that the temperature disturbance due to

bathymetry decays exponentially with depth, and penetrates deeper for longer wavelength terrain. The magnitude of the disturbance is proportional to the amplitude of the terrain and the magnitude of the water-temperature gradient.

In reality, the bathymetry at the core sites is more complicated than this simple two-dimensional structure, and the temperature perturbation at depth cannot be solved for analytically. Instead, the three-dimensional effects of bathymetric relief are calculated numerically according to the Fourier-series continuation technique described by *Blackwell et al.* [1980]. This correction quantifies thermal perturbations due to bathymetry from two sources, 1) the change in average bottom water temperature (ΔBWT) as a function of depth and 2) perturbations to the thermal gradient due to bathymetric relief. For each site, temperatures are calculated over a 2 x 2 km bathymetry grid surrounding the borehole, where the grid resolution is 225 x 225 m. The effects of bathymetry beyond this region are minimal.

The correction first requires constructing a horizontal reference grid along a plane that passes through the level of the seafloor at the location of the borehole. Temperature differences at each grid cell along this reference plane are computed for the two effects. $\Delta T(x,y)$ due to BWT is determined by extrapolating temperatures from nearby CTD casts from the NOAA World Ocean Database to the bathymetry grid and subtracting these values from the temperature at the depth of the surface of the borehole. Temperature differences due to uneven surface bathymetry are estimated by multiplying the observed subsurface temperature gradient ($\Gamma_{obs} = dT/dz$) by the difference in height Δz between the grid elevation and the reference plane. These two temperature difference grids are summed together and then upward continued, where z is positive down, to compute the temperature perturbation in the subsurface due to bathymetry. The actual gradient is determined through an iterative procedure using the secant method, with a stopping criteria that minimizes the difference between the observed and predicted temperatures. The bathymetric correction, as a percent, is given by the ratio of the corrected and observed gradient ($\Gamma_{corr}/ \Gamma_{obs}$).

The bathymetric correction calculations for site U1413 are illustrated in Figure 6. This site is located in a local valley at a depth of ~540 mbsf (Figure 6a). The depth of the 2 x 2 km grid surrounding this site varies between 450 and 650 mbsf. Seafloor temperatures are estimated by fitting the mean water temperature-depth profile (Figure 6b) to the bathymetry. The BWT at this

site is 8.9° C and varies between 7.7 and 10.3° C over the depth range of the grid. Figure 6c shows the difference in these temperatures relative to the borehole BWT. The second component of the correction accounts for the bathymetry by computing temperature differences relative to the borehole due to the overlying or underlying bathymetry (Figure 6d). The sum of these two components is shown in Figure 6e. This grid is upward continued into the subsurface and the corrected gradient is determined iteratively. The corrected gradient is 3% lower than the observed gradient (Table 4), consistent with the site's position in a local valley.

In general the thermal effect due to bathymetry is much larger than the effect due to BWT. For sites below 2000 m, BWT variations are very small (<0.5 °C/km) (Figure 6b). Heat flow values corrected for bathymetry are reported in Table 4. Corrections for all sites are all less than 6%. Sites U1378, U1381, and U1412 are located on local seafloor highs and the correction increases the thermal gradient. Site U1413 and U1414 are located on local lows and the corrections decrease the gradients. The largest bathymetric corrections are on the oceanic plate sites (U1381 and U1414), where the Cocos Ridge contributes to rough seafloor bathymetry.

3.4.2 Sedimentation Corrections

As sediments are deposited on the seafloor they are assumed to be in equilibrium with the bottom water temperature. Rapid sediment accumulation can transiently depress near-surface heat flow until the sediment warms to background values. The effect of sedimentation on the thermal gradient is shown in Figure 7. Prior to sedimentation, temperature increases with depth along a constant conductive gradient G_0. If a package of sediment is instantaneously deposited at time t = 0, it initially has an isothermal profile at the bottom water temperature. As time progresses, the thermal field warms to the new background condition shown by the line at $t = \infty$.

The thermal effects of sedimentation are greatest for the most recent large sedimentation events that are preserved in the uppermost sedimentary layers. Mass accumulation rates are estimated from calcareous nannofossils, radiolarians, planktonic foraminifera and paleomagnetic data [*Vannuchi et al.* 2012*; Harris et al*. 2013]. The sediment age-depth relationship for each drilling site was constructed using estimated sediment accumulation rates reported in IODP proceedings (Figure 8a, Table 2). In general, mass accumulation rates are low on the incoming plate, and very high on the upper plate (Table 2). Recent accumulation rates on the margin slope

are large, varying between 516 m/Myr on the middle slope to 1035 m/Myr on upper slope site U1379. These rapid depositional rates may be the result of enhanced uplift and erosion of the Osa Peninsula as the overthickened, buoyant Cocos ridge impinged on the margin, as well as increased margin subsidence due to subduction erosion, which created a basin that makes space for deposited sediment [*Vannuchi et al*., 2013].

The thermal impact of sedimentation on observed heat flow values is estimated using SlugSed, a one-dimensional numerical model of fluid and heat transport [*Hutnak and Fisher,* 2007]. This model simulates heat transport with a deforming finite difference grid. As sediment is added, new nodes are generated and the sediment-basement interface moves downward. The accumulating sediment layer follows a user-specified porosity-depth relation, $\phi(z)$, and bulk sediment thermal conductivity and permeability depend on this porosity function. The porosity-depth function is specified according to Athy's law [*Athy*, 1930].

$$\phi(z) = \phi_0 exp(-z/L_c) \tag{4}$$

where ϕ_0 is the initial porosity at the surface, and L_c is an empirically derived compaction constant. These constants were determined by fitting Athy's law to the porosity-depth data at each site (Figure 8, Table 2). With the exception of Sites U1381 and U1414, Athy's law fits the porosity depth data well. A porosity inversion at Site U1381 occurs at the hemipelagic-pelagic boundary, which corresponds to a depositional hiatus. The poor fit at Site U1414 is attributed to a gas disturbance.

Thermophysical parameters used in SlugSed are summarized in Table 3. Figure 8b shows normalized variations in heat flow for the mass accumulation rates given in Table 2. The seaward and toe sites have low sedimentation corrections (< 10%) while the margin sites have relatively large corrections (10-30%). Site U1379 has the highest correction because it experienced an extremely rapid mass accumulation rate (>1000 m/My) in the past half million years (Figure 8a).

3.4.3 Summary of Heat Flow Corrections

The sedimentation corrections are more predominate than the bathymetric corrections, with the net result of increasing heat flow relative to observations (Table 4, Figure 10). Sediment corrections are largest for upper and middle slope sites where sedimentation rates have been particularly high over the past 1.5-2Ma. Corrected values of heat flow decrease from 195 mW/m^2 on the oceanic plate (Site U1381) and to 46 and 53 mW/m^2 at the upper slope Sites U1413 and U1379, respectively. This landward decrease in heat flow is consistent with downward advection of heat by subduction. Both oceanic plate sites (U1381 and U1413) have higher heat flow values than the predicted value of 128 mW/m^2 based on conductive plate cooling models for 16 Ma crust [*Stein and Stein*, 1992]. These anomalously high values are consistent with the presence of convective fluid flow within a crustal aquifer. The particularly high heat flow on site U1381 is likely due to its position on a local basement high, where the relief focuses fluid flow, and the thin sediment cover provides limited thermal insulation.

4 Thermal Model

The heat flow measurements provide a valuable first-order constraint for understanding the thermal regime of the margin. In this section, I construct thermal models of the subduction zone to better understand the parameters that affect the thermal structure of the margin. Thermal models in this study build on results developed for this region by *Harris et al.* [2010b], who found that heat flow profiles along the southern Costa Rica margin are consistent with thermal models that incorporate insulated hydrothermal circulation within the uppermost layer of the oceanic crust that is composed of pillow basalt. I explore variations on this basic structure, specifically looking at the effects of plate geometry, convergence rate, the permeability structure of the aquifer, and the coefficient of friction along the plate boundary.

4.1 Thermal Model Description

The temperature regime of the shallow subduction zone is largely a function of the thermal state of the incoming plate, the convergence rate, geometry, and the thermal properties of the margin [e.g., *Dumitru,* 1991]. The thermal structure of the of the margin along the CRISP transect is modeled using the 2-D finite-element model developed by *Wang et al.* [1995] that solves the heat transfer equation for a subducting slab under steady state conditions,

$$\rho c \frac{\partial T}{\partial t} = \nabla \cdot (\mathrm{k}\nabla \mathrm{T}) - \rho c v \cdot \nabla \mathrm{T} + Q, \tag{5}$$

where T is temperature as a function of landward distance, x, from the deformation front and depth, z, below sea-level. Here, k is thermal conductivity, ρc is volumetric heat capacity, ν is velocity, and Q is a heat source term arising from the radiogenic heat production of the rocks and from frictional heating. The velocity term within the subducting slab is the convergence rate of the Cocos plate relative to a fixed Caribbean plate. Flow within the mantle induced by the subducting slab is approximated using an analytical corner flow solution where the mantle wedge is assigned an isoviscous rheology coupled to the subducting slab [*Peacock and Wang*, 1999; *Batchelor*, 1967]. Heat transfer is advective within the upper subducting oceanic crust, and conductive through the forearc.

4.1.1 Model Geometry and Thermal Physical Rock Properties

The model consists of five main geometric units with differing thermophysical properties: a 100 km thick oceanic plate, 100 m of incoming sediment, an accretionary prism, 40 km thick island arc crust (Choretoga block), and mantle wedge (Figure 11). The plate boundary is defined using seismic reflection and refraction data, Wadati-Benioff earthquakes, and tomographic images of the slab [*Ranero et al*., 2005]. The depth to the shallow portion of the slab is determined from an updated model of relocated epicenters of aftershocks of the 1999 Quepos earthquake [*Kyriakopoulos et al*., in press]. The upper plate Moho is set to a depth of 40 km [*DeShon et al.* 2006*; MacKenzie et al*. 2008]. Thermophysical parameters for each model unit

are summarized in Table 5. These parameters are the same as those used by *Harris et al*. [2010b] and are consistent with previous thermal studies of subduction zones [e.g., *Hyndman and Wang,* 1993*; Currie et al.* 2002;].

Previous studies of the oceanic crust offshore Costa Rica have shown evidence for hydrothermal circulation within the uppermost layer of oceanic crust, comprised of permeable sheet flows and pillow basalts with an estimated regional scale permeability on the order of 10^{-9}-10^{-10} m^2 [*Fisher,* 1998]. Below this layer, underlying sheeted dykes have permeability estimated to be several orders of magnitude lower (~10^{-17} m^2) that does not support hydrothermal circulation. This study investigates the role of hydrothermal circulation within a 600 m thick permeable aquifer [*Spinelli and Saffer*, 2004; *Hutnak et al.*, 2007].

4.1.2 Boundary Conditions

Subduction zone temperatures are highly sensitive to the thermal state of the incoming oceanic crust. This study explores two initial geotherms for models excluding and including hydrothermal circulation within a permeable upper oceanic aquifer. For solutions that do not incorporate fluid flow within the upper oceanic aquifer, the initial seaward boundary condition is defined according to half-space cooling models of a 16 Ma plate with 100 m of sediment cover, shown in the left panel of Figure 11. For solutions including a permeable aquifer, the thermal profile is conductive within the 100 m of sediment, isothermal within the aquifer, and defined by half-space cooling below the aquifer. In both cases, the seafloor temperature is set to 0° C, and the temperature at the bottom of the 100 km thick subducting lithosphere is set to 1400° C. The landward boundary condition is defined by surface heat flow of 70 mW/m^2 through the upper and lower plate (Choretoga block), consistent with a back-arc setting, and an adiabatic gradient through the mantle wedge. This condition is set at 300 km landward of the trench, sufficiently far from the seismogenic zone to avoid boundary effects.

4.2 Hydrothermal Circulation within Oceanic Basement Aquifer

The effects of hydrothermal circulation within the upper oceanic aquifer are modeled with a Nusselt number approach [*Spinelli & Wang*, 2008, 2009; *Kummer and Spinelli*, 2008, 2009] that

uses a conductive proxy to simulate the thermal effects of convection. Advective heat transfer within the permeable aquifer is simulated by increasing the thermal conductivity by a factor *Nu,* defined as the ratio of total heat transport, q_{total}, to heat that would be transferred by conduction alone. The effective thermal conductivity in the aquifer, λ_{eff}, is computed from the Nusselt number according to

$$\lambda_{eff} = Nu * \lambda_{cond}, \tag{6}$$

Nu is quantitatively estimated by first calculating the Rayleigh number, *Ra*, a dimensionless measure of the ratio of thermal buoyancy to viscous resistance to flow. *Nu* and *Ra* are determined through an iterative procedure. Temperatures are first modeled for the conductive case, without incorporating fluid circulation. These modeled temperatures are used to initialize heat flux in the base of the aquifer. Temperature-dependent values of fluid density (ρ), thermal expansivity (α), viscosity (μ), and thermal diffusivity (κ), are computed throughout the aquifer. These values, along with a prescribed depth-dependent permeability (k) and aquifer thickness h (600 m), are used to compute *Ra*,

$$Ra = \frac{\rho g \alpha k h^2 q}{\mu \kappa \lambda}. \tag{7}$$

where g is the acceleration of gravity [*Spinelli and Wang*, 2008]. The Nusselt number is related to the Rayleigh number, through

$$Nu = 0.08 Ra^{0.89}, \tag{8}$$

a relationship empirically determined by comparing results using the conductive Nusselt proxy for fluid flow to results from simulations incorporating coupled heat and fluid flow [*Kummer and Spinelli*, 2008]. New temperatures are computed for the effective thermal conductivity, and the procedure is repeated until temperatures stabilize, which occurs within 5 iterations.

4.2.1 Permeability Structure of Basement Aquifer

While evidence for the presence of hydrothermal circulation is fairly well established in CNS crust, the permeability structure of the upper oceanic basement aquifer is still poorly known. This section investigates the sensitivity of modeled surface heat flow to the order of magnitude permeability and depth of hydrothermal circulation within the uppermost oceanic crust.

The preferred thermal model for the southern-most Costa Rica transects generated by *Harris et al.* [2010b] incorporated an aquifer permeability that exponentially decreases with depth according to the relationship $\log(k) = -9 - 5.5\times10^{-5(z-600m)}$. This function was based on values used by *Spinelli and Wang* [2008] for the Nankai margin. Here, I test two sets of permeability structures within the 600 m thick aquifer: 1) a constant permeability to a fixed depth, which then drops to advectively impermeable values below the cutoff depth, and 2) an exponentially decreasing permeability described by $\log(k) = -a - b*10^{-5(z-600m)}$, where the constant a represents the permeability at the surface and b controls the rate at which permeability decreases with depth. The decrease in permeability is consistent with expected depth-dependent metamorphic phase changes, where minerals produced at facies boundaries chemically and mechanically seal pores and fractures [e.g. *Spinelli & Wang*, 2008].

Figure 12 shows the aquifer permeability structure for each case that produce a relatively good fit between modeled and observed data. The left panels (a and c) are for the case of fixed permeability to a set cutoff depth, and the right panels show the case of exponentially decreasing permeability. The top panels, 12 a and b, show the specified permeability, and the bottom panels (c and d) show the calculated effective thermal conductivities computed from the Nusselt number technique. The effective thermal conductivity within the aquifer reaches maximum values on the order of 10^3 W/m/K, three orders of magnitude larger than typical rock conductivities. This results in an essentially isothermal temperature profile within the aquifer, as would be expected with high Rayleigh number convection.

Models incorporating hydrothermal circulation using the Nusselt-number approximation, shown in red in Figures 13a and 13b, predict higher surface heat flows near the trench and a steeper landward decrease in heat flow than do models including a conductive aquifer, shown in black. This result is consistent with advective redistribution of heat from deeper portions of the

thrust to the trench. These Nusselt models provide a better fit to the heat flow profile observed along the CRISP transect, and the model is most sensitive to the specified aquifer permeability.

In order to constrain the permeability of the uppermost basement, I calculated the root mean square (RMS) misfit between the modeled and observed surface heat flow values, which included the data from the cores determined in the first part of this study, combined with BSR and marine-probe heat flow values reported by *Harris et al.* [2010b]. All model variables are fixed except for two free parameters pertaining to the permeability structure. Contour plots of the RMS misfit between observed and modeled surface heat flow data are shown for the two permeability structures in Figures 13c and 13d. BSR heat flow values that drop off landward of 10 km were removed before RMS calculations were made. To emphasize the reliability of downhole heat flow values, these values were more heavily weighted than BSR and marine-probe values. The weighted RMS calculations favor a model that more closely matches the high heat-flow value measured at oceanic plate site U1381.

The RMS misfit of the permeability step function (Figure 13a and 13b) shows that this model is sensitive to the aquifer permeability and relatively insensitive to the maximum depth of circulation. A fairly wide range of cutoff depths fit the data equally well, as shown by the large minimum RMS contour interval. Models incorporating aquifer permeabilities between approximately $10^{-9.4}$ - $10^{-9.7}$ m^2 and cutoff depths between 10 and 20 km yield reasonable fits to the observed data. Models incorporating lower permeabilities and shallower cutoff depths under-predict heat flow observations near the trench, yielding a heat flow structure similar to conductive predictions (i.e. no fluid flow). Higher permeabilities and deeper circulation result in surface heat flow values that over-predict observed values at the trench. The best fitting permeability of this form is $10^{-9.5}$ m^2 with a maximum depth of circulation of 15 km (Figure 12b). This circulation cutoff depth corresponds to a modeled thrust temperature of ~130° C.

The RMS misfit contours using the exponentially decreasing permeability function are shown in Figure 13d. Here the RMS minima contour is oblique indicating an inverse correlation between the surface permeability and the rate of permeability decay with depth. The permeability structure of this form that best fits the observed data is $\log(k)=-9.5-5*10^{-5(z-600m)}$. This permeability function drops off to an advectively impermeable value of 10^{-13} m^2 at a depth of 70 km (Figures 12b, 13b). This depth corresponds to a subduction thrust temperature of ~300° C.

Figures 13 a and b show modeled surface heat flow results for the best-fitting permeability structures in red. Both preferred permeability models yield similar RMS misfits to the observed heat flow data, indicating that the permeability structure is non-unique.

The remainder of the study explores models with the best-fit exponentially decreasing permeability function shown in Figure 12b, inset. This structure is likely more physically reasonable than an abrupt step-drop in permeability. While the preferred model fits values seaward of 15km fairly well, it underestimates heat flow observations at the two most seaward (upper slope) sites U1379 and U1413 by over 20 mW/m^2.

4.3 Frictional Heating

Models generated thus far have not incorporated the effects of frictional heating along the subduction thrust. Although frictional heat along the seismogenic portion is only dissipated when the fault is in motion, heat flow measured at the surface is assumed to reflect the frictional heat integrated over numerous earthquakes [*Gao and Wang*, 2014]. The thermal state of the thrust fault is sensitive to frictional heating, however the effective coefficient of friction of thrust faults is not well established [e.g. *Molnar and England,* 1995, *Currie et al.*, 2002]. Evidence from thermal modeling and geo-mechanical laboratory tests suggest that the coefficient of friction has a low value [*Wang et al.*, 1995, *Hyndman*, 2007].

The coefficient of friction governs the generation of heat along the plate interface and its effect is investigated following methods implemented by *Wang et al.* [1995]. In the brittle regime, the frictional heat per unit fault width, Q_f, for a sliding velocity, v, can be expressed as,

$$Q_f = \tau v = \mu' \sigma_n v, \tag{9}$$

where τ is the shear stress, and μ' is the effective coefficient of friction on the fault plane, and σ_n is normal stress across the fault. Normal stress increases with depth proportional to the weight of the overlying material. In the ductile regime, the magnitude of heating per unit volume is given by the product of the shear stress and strain rate, $\dot{\varepsilon}$,

$$Q_f = \tau\dot{\varepsilon}. \quad (10)$$

The viscous stress is determined from the strain rate using the power law rheology for diabase [e.g., *Caristan*, 1982]. The magnitude of shear stress decreases with depth as temperature increases. Below the Moho, at 40km depth, the interface between the down going plate and the serpentinized mantle wedge is believed to be too weak to generate significant heating [e.g., *Currie et al.,* 2002].

Models incorporating higher aquifer permeabilities result in lower thrust temperatures landward of the trench. Conversely, a higher coefficient of friction, which essentially acts as an additional heat source term, increases thrust temperatures. Thus there is a tradeoff between these two model parameters, aquifer permeability and coefficient of friction. In order to better constrain interface friction and aquifer permeability, I computed the RMS misfit between observed and modeled heat flow for different combinations of these two variables, and contoured these values, shown in Figure 14. Models incorporate an aquifer permeability structure that follows the form $\log(k) = -k_0 - 5*10^{-5(z-600m)}$, where the surface permeability k_0 varies from 10^{-9} to $10^{-10.5}$ m^2. The minimum contour interval shows the combination of parameters that best fit the data (RMS <15 mW/m^2). If the model includes no frictional heating, the best fitting surface permeability is between $10^{-9.5} – 10^{-9.7}$ m^2. Models incorporating a coefficient of friction of up to 0.05 fit the observed heat flow if the aquifer has a lower surface permeability (10^{-10} m^2). This coefficient of friction comparable with values determined along the Tohoku-Oki fault determined from a borehole temperature observatory installed months after the 2011 earthquake [*Fulton et al.*, 2013].

4.4 Sensitivity of Thrust Temperatures to Model Parameters

Now that a range of reasonable values for aquifer permeability and coefficient of friction along the plate interface has been established, this section explores how small perturbations in these model parameters affect the temperatures along the plate interface, which is thought to control the seismogenic portion of the fault (Figure 15). I also explore the sensitivity of the modeled heat flow and thrust temperatures to reasonable variations in plate age and convergence

rate (Figure 15). Since the updip limit of interplate seismicity is inferred to occur between temperatures of 100 - 150° C, I also look at the sensitivity of the position of these modeled temperatures along the subduction thrust.

Surface heat flow is highly sensitive to aquifer permeability, particularly at distances <10 km landward of the trench. Figure 15 a-c show the sensitivity of the model results to variations in aquifer surface permeability between 10^{-9} -10^{-10} m^2 , i.e. parameter a varies from 9 to 10, where permeability is specified by log(k)= -a -5*$10^{-5(z-600m)}$. The presence of hydrothermal circulation within the aquifer suppresses thrust temperatures at depth, and increases temperatures close to the deformation front (Figure 15b). A lower aquifer permeability aquifer results in higher thrust temperatures, and shifts the position of the 100°- 150° C thrust temperatures updip (Figure 15c). Decreasing the surface permeability from $10^{-9.5}$ to 10^{-10} m^2 shifts the 100°- 150° C thrust temperatures landward 5 km, and 2-3 km shallower, respectively.

Including frictional heating warms the thrust without significantly affecting the surface heat flow. Figure 15 d-f show the sensitivity of the model to a coefficient of friction varying between 0.02 and 0.04, where permeability is specified by log(k)= -9.5 -5*$10^{-5(z-600m)}$. A 33% increase in the coefficient of friction (i.e. from 0.03-0.04) increases surface heat flow by at most 6%, but can increase the temperature by as much as 55°C (~14%). The increase in temperature due to the higher coefficient of friction is more exaggerated further downdip (i.e. further landward), however, and is not as pronounced at shallower portions of the thrust where the updip limit of seismicity occurs. This temperature increase corresponds to a 3 km seaward and 1-2 km shallowing of the 100° C and 150° C isotherms (Figure 15f). Because surface heat flow is relatively insensitive to variations in friction, but temperatures along the subduction thrust are sensitive to small variations in the coefficient of friction, it is difficult to establish the coefficient of friction from surface heat flow data alone.

A younger incoming plate results in slightly higher surface heat flow and elevated subduction thrust temperatures (Figure 15 g-i) due to the increased heat content of the plate. Varying the plate age by ± 2 Ma (~12 %) leads to a change in the surface heat flow of about 10% and a change in subduction thrust temperatures of about 11% (< 14° C). The surface heat flow is more sensitive to variations in age near the trench than it is deeper along the thrust, while subduction thrust temperatures are more perturbed further downdip. The 2 Ma increase in age shifts the

intersection of the 100° and 150° C isotherm with the subduction thrust approximately 6 and 4 km landward (6%), respectively and 6 and 5 km deeper (6%), respectively (Table 6).

A faster converging plate results in a slightly cooler thrust and lower surface heat flow (Figure 15 j-k). This is due to the more rapid subduction of the relatively cool oceanic slab. Varying the convergence rate by ± 20 mm/yr (~20%) leads to a change in surface heat flow of less than 5% and a change in thrust temperatures of less than 6%. Interestingly, models with a 20% lower convergence rate yield a slightly better RMS misfit to observed data (Table 6), consistent with recent MORVEL model estimates of a convergence rate of 79.6 mm/yr in this region [*DeMets et al.*, 2010].

In summary, the modeled surface heat flow is most sensitive to the presence and extent of hydrothermal circulation within the permeable aquifer, while the modeled thrust temperature is highly sensitive to the coefficient of friction. The temperatures at the updip portion of the thrust, however, (top 20 km) are less affected by the coefficient of friction, that the deeper portions, and an increase in coefficient of friction will only shift the updip isotherms seaward by a small percentage. The sensitivity trade-off plots (Figures 13 and 14) demonstrate that there is not a unique solution that fits the observed data, however, surface permeability is fairly well constrained to between $10^{-9.5} – 10^{-10}$ m^2, and the coefficient of friction is likely < 0.05.

4.5 Correlation between Modeled Thrust Temperatures and Interplate Seismicity

Based on the estimated parameters, I selected two preferred thermal models to approximate the temperature structure of the thrust, the first excluding frictional heating, and the second including friction with a coefficient of 0.03. Both preferred models are for a 16 Ma plate that is converging at 97.1 mm/yr with 100 m of sediment cover, and include a 600 m thick oceanic aquifer whose permeability decreases with depth below seafloor according to the function $\log(k) = -9.5 - 5*10^{-5(z-600m)}$.

In order to correlate the modeled thrust temperatures with seismicity, I estimate the position of the updip limit of seismicity from relocated seismic events reported by *DeShon et al.* [2003] and *Arroyo et al.* [2014]. Seismicity includes aftershock events from the 1999 M_w 6.9 Quepos earthquake recorded by the Osa component of the CRSEIZE experiment, as well as aftershocks

events from the 2002 M_w 6.4 Osa Earthquake. Events within 5 km of the CRISP transect are projected onto the thrust cross-section, and interplate seismicity is defined to be within ± 5 km of the thrust (Figure 16). The updip limit of seismicity is estimated to be at a landward distance of 15 km and a depth of 5-10 km (Figure 16, left inset). Temperatures of these hypocenters are approximated for each thermal model from interpolation, and binned in 25° C intervals in order to approximate the updip temperature range for each model (Figure 16 middle and right insets). The updip limit temperature of seismicity to be between 50-75° C for models including and excluding frictional heating. This temperature range is cooler than 100-150° C temperatures correlated with the updip limit of seismicity at accretionary subduction zones [e.g., *Hyndman and Wang*, 1993; *Oleskevich et al*., 1999].

Figure 17 shows thrust temperatures for the two preferred thermal models. Model A does not incorporate any frictional heating, and Model B includes a coefficient of friction of 0.03. For comparison I also show the plate interface temperature models of *Ranero et al.* [2008] and *Harris et al.* [2010b]. *Ranero et al.* [2008] predicted temperatures are based on downward extrapolations of surface heat flow, and result in a distinctly warmer thrust. This model is likely too warm because it neglects the advection of heat with the downgoing slab [e.g., *Molnar and England*, 1995]. The new models are cooler than that of *Harris et al.* [2010b] within 20 km of the trench but are relatively warmer with landward distance. The primary difference between these models is the new plate interface developed by [*Kyriakopoulos et al.,* in press], which has an initially steeper dip than that used by Harris et al. [2010b]. Relative to the model temperature of *Harris et al.* [2010b], Model A shifts the intersection of the 100° and 150° C isotherms with the thrust 3-15 km seaward, respectively, and Model B shifts these isotherms 15-30 km seaward.

5 Discussion

According to the thermal model results from this study, the updip limit of seismicity is correlated with cooler temperatures of 50-75° C than the updip thrust temperatures of 100-150° C typically observed at accretionary subduction zones [e.g., *Hyndman and Wang*, 1993; *Oleskevich et al*., 1999]. As the sensitivity tests indicate, one way to increase the temperature on the subduction thrust would be to increase the coefficient of friction. Associating the updip limit

of seismicity with 150° C would require a coefficient of friction to be at least 0.1, a value higher than commonly inferred [*Di Toro et al*., 2004] or observed [*Fulton et al.*, 2013]. Additionally, a coefficient this high would provides a poorer fit to the observed surface heat flow data, particularly near the trench (Figure 14, 15a).

At accretionary margins, models invoked to explain the temperature control of the updip limit of seismicity include: 1) alteration in clay frictional properties as hydrous smectite dehydrates to anhydrous illite, which was thought correspond to a change from velocity strengthening to velocity weakening behavior [*Hyndman et al*., 1997]; and 2) declining fluid production and decreasing fluid pressure ratio resulting in an increase in normal stress, strengthening of the hanging wall and an onset of velocity weakening behavior [*Moore and Saffer*, 2001]. The first model is now disfavored because laboratory experiments on the frictional behavior of clays indicate that illite is not velocity weakening [*Saffer and Marone*, 2003]. Smectite, a major source of fluid after decompaction, dehydrates to illite at temperatures between 80° and 150° C and therefore our models predict that fluid sources will be dehydrating at the modeled temperature of the updip limit of seismicity. A third model posits that the transition from aseismic to seismic behavior results from increasing lithification with depth, which leads to a shift from pervasive shear to localized shear within the fault zone [*Marone and Scholz*, 1988; *Davis et al.*, 1994]. This model is not explicitly controlled by temperature, though some lithification processes are at least partially mediated by temperature.

In the CRISP drilling region, shallow seismicity is correlated with the subduction of bathymetric relief [*Husen et al.*, 2003; *Bilek et al*., 2003; *DeShon et al.*, 2003]. *Bilek et al.* [2003] demonstrate that seismicity in this area occurs in patches elongated downdip and with rupture areas matching the width of incoming bathymetric features such as the Quepos Plateau. Additionally, bathymetric highs in this area are capped by nannofossil chalk [*Spinelli and Underwood*, 2003], which *Ikari et al.* [2013] found to be velocity weakening.

I envision the plate boundary, in the region of the CRISP drilling transect, as a corrugated surface in which bathymetric highs capped with nannofossil chalk form the peaks and troughs are filled with hemipelagic and pelagic clays. As high bathymetric features are subducted, they gouge the frontal prism, thereby frontally eroding the margin, and the plate boundary must pass over the seamounts and through the nannofossil chalk unit. Because nannofossil chalk is

velocity weakening from the outset, it is possible for seismicity to occur at a shallow level along the thrust independent of temperature. As the seamounts pass deeper into the subduction zone, the system becomes stiffer and can store elastic strain required for an earthquake. In this way the aseismic/seismic transition associated with bathymetric highs could occur updip of the intersection of the 100-150° C isotherms with the subduction thrust. I suggest that at the shallowest levels of observed seismicity, regions of velocity weakening chalk capped bathymetric highs alternate with velocity strengthening dehydrating hemipelagics that infill bathymetric lows. These spatially variable frictional properties contribute to the observed patchiness of seismicity. If the onset of seismicity associated with the hemipelagics occurs at temperatures of 150° C, then these areas would start rupturing at a depth of ~30 km.

It is interesting to compare the results reported here offshore the Osa Peninsula with those from offshore the Nicoya Peninsula, where relatively smooth seafloor is being subducted. At the Nicoya Peninsula (Figure 1) a plate suture juxtaposes anomalously cold crust (10-20 mW/m^2) formed at the EPR against warmer much warmer CNS crust (100-120 mW/m^2). The anomalously low heat flow values are attributed to vigorous hydrothermal circulation within a ventilated oceanic crust [e.g., *Langseth and Silver*, 1996; *Harris and Wang*, 2002; *Fisher et al.,* 2003; *Hutnak et al.*, 2007]. *Newman et al.* [2002] relocated 650 earthquakes along the plate interface using a dense seismic network offshore the Nicoya Peninsula and found that the updip limit of seismicity transitioned from a depth of 10 km on the warm CNS side to a depth of 20 km on the cold EPR side. *Harris and Wang* [2002] show that these depths correspond to temperatures of 100 to 150° C, consistent with the hypothesis that thermally mediated processes in this temperature range control the updip limit of seismicity.

Thus it appears that the updip limit of seismicity is influenced by temperature at the Nicoya Peninsula but not at the Osa Peninsula. The hypothesis that the updip limit of seismicity appears to be a function of subducting bathymetric relief is consistent with along strike changes in the bathymetry of the incoming plate. With progressively higher relief along the southern part of this margin (Figure 1), there is increasing evidence of frontal erosion, such as seamount scars in the frontal prism [*von Huene et al*., 2000]. These results emphasize the importance of frictional heterogeneities along the subduction thrust due to bathymetric relief [*Bilek*, 2007]. Globally, this

heterogeneity may be more pronounced at erosive convergent margins where the incoming sediment thickness is small relative to the size of bathymetric relief.

6 Conclusions

Analysis of heat flow values collected during IODP coring expeditions offshore the Osa Peninsula provide new insight into the thermal state of the southern Costa Rica subduction zone. This margin represents an erosive end-member margin style with low sediment cover and high bathymetric relief associated with the Cocos Ridge. On the basis of this study, I make the following conclusions:

1) Along the CRISP drilling transect heat flow corrected for the effects of bathymetry and sedimentation decreases from ~210 mW/m^2 on the incoming plate to ~50 mW/m^2 on the upper slope. Bathymetric corrections to heat flow are generally small whereas corrections for the effects of sediment can be relatively large with a maximum correction of 32%. The landward decrease in heat flow is consistent with the downward advection of heat by the subducting plate.

2) Heat flow determined from IODP holes are generally consistent with those determined from marine probes and bottom simulating reflectors. This consistency suggests that heat transfer in the shallow upper plate is largely conductive.

3) Heat flow values on oceanic sites are higher than half-space cooling model predictions for 16 Ma crust, and the elevated values are consistent with hydrothermal circulation that advects heat to the surface through a permeable crustal aquifer.

4) Thermal models of subduction that incorporate hydrothermal circulation within a 600 m thick upper oceanic permeable basement aquifer successfully predict the large heat flow values near the trench and the sharp decrease of heat flow landward of the trench. Hydrothermal circulation warms the subduction thrust near the trench and cools the subduction thrust landward of the trench. Best fitting models incorporated an exponentially decreasing aquifer permeability

structure of the form $\log(k)=-9.5-5*10^{-5(z-600m)}$. The extent of advective circulation as defined by permeabilities $< 10^{-13}$ m^2 occurs at a depth and temperature of 70 km and 300° C, respectively.

5) There is a tradeoff in model parameters between the coefficient of friction and surface aquifer permeability. The coefficient of friction along the plate interface is likely < 0.05, however it is difficult to constrain from heat flow data alone.

6) Modeled plate interface temperatures associated with earthquake relocations suggest that the updip limit of seismicity occurs between 50° -75° C. This temperature range is significantly lower than the 100-150°C range required for a temperature-mediated control of the updip limit of seismicity. Instead I argue that the presence of velocity weakening nannofossil chalk on bathymetric highs is controlling the updip limit of seismicity in this erosive margin.

7 References

Arroyo, I. G., Grevemeyer, I., Ranero, C. R. and von Huene, R. (2014), Interplate seismicity at the CRISP drilling site: The 2002 Mw=6.4 Osa Earthquake at the southeastern end of the Middle America Trench, *Geochem. Geophys. Geosyst*., *15* (7), 3035-3050, doi: 10.1002/2014GC005359.

Athy, L.F., (1930), Density, porosity, and compaction of sedimentary rocks, *AAPG Bull.*, *14*, 1-24.

Bangs, N. L., K. D. McIntosh, E. A. Silver, J. W. Kluesner, and C. R. Ranero, (2014), Fluid accumulation along the Costa Rica subduction thrust and development of the seismogenic zone, *J. Geophys. Res. Solid Earth*, *120*, 67-86, doi:10.1002/2014JB011265

Barckhausen, U., C. R. Ranero, R. von Huene, S. C. Cande, and H. A. Roeser (2001), Revised tectonic boundaries in the Cocos Plate off Costa Rica; Implications for the segmentation of the convergent margin and for plate tectonic models, *J. Geophys. Res*., *106*, 19, 207-220, doi:10.1029/2001JB000238.

Beardsmore, G. R. & Cull, J. P. 2001. Crustal Heat Flow. A Guide to Measurement and Modeling. x + 324 pp. Cambridge, New York, Melbourne: Cambridge University Press.

Bevington, Philip R., and D. Keith Robinson, (2003), *Data reduction and error analysis*, *McGraw–Hill, New York.*

Bilek, S. L., and T. Lay (1998). Variation of interplate fault zone properties with depth in the Japan subduction zone, *Science*, 281, 1175-1178.

Bilek, S. L., S. Y. Schwartz, and H. R. DeShon (2003), Control of seafloor roughness on earthquake rupture behavior, *Geology*, *31*(5), 455–458, doi:10.1130/0091-7613(2003) 031<0455:COSROE>2.0.CO;2.

Bilek, S.L., (2007), Influence of subducting topography on earthquake rupture, in *The Seismogenic Zone of Subduction Thrust Faults*, ed. T. Dixon and C. Moore, Columbia University Press, pg. 123-146.

Blackwell, D. D., J. L. Steele, and C. A. Brott (1980), The terrain effect on terrestrial heat flow, *J. Geophys. Res*., *85*(B9), 4757–4772, doi:10.1029/JB085iB09p04757.

Bullard, E.C., (1939), Heat Flow in South Africa. *Proc. of the Royal Society A-Mathematical Physical and Eng. Sci*., *173*, 474-502, doi:10.1098/rspa.1939.0159

Caristan, Y. (1982), The transition from high temperature creep to fracture in Maryland diabase, *J. Geophys. Res*., *87*, 6781–6790, doi:10.1029/JB087iB08p06781.

Carslaw, H.S., and J.C. Jaeger (1959), Conduction of Heat in Solids, 2nd edition, Oxford University Press, Oxford, 510 p.

Clift, P., and P. Vannucchi (2004), Controls on tectonic accretion versus erosion in subduction zones: Implications for the origin and recycling of the continental crust, *Rev. Geophys*., *42*, RG2001, doi:10.1029/2003RG000127.

Currie, C. A., R. D. Hyndman, K. Wang, and V. Kostoglodov (2002), Thermal models of the Mexico subduction zone: Implications for the megathrust seismogenic zone, *J. Geophys. Res*., *107*(B12), 2370, doi:10.1029/2001JB000886.

Davis, D. M., et al. (1994), Porosity loss in the evolution of accretionary wedges; some mechanical and seismic implications, in *Proceedings of the Workshop LXIII, USGS Red-Book Conference on the Mechanical Involvement of Fluids in Faulting, U.S. Geol. Surv. Open File Rep.*, 94-0228, 460-465.

Davis, E. E., K. Wang, J. He, D. S. Chapman, H. Villinger, and A. Rosenberger (1997), An unequivocal case for high Nusselt-number hydrothermal convection in sediment buried igneous oceanic crust, *Earth Planet. Sci. Lett*., *146*, 137–150, doi:10.1016/S0012-821X(96)00212-9.

DeMets, D. C. (2001), A new estimate for present-day Cocos-Caribbean plate motion: Implications for slip along the Central American volcanic arc, Geophys. Res. Lett., 28, 4043–4046, doi:10.1029/2001GL013518.

DeMets, C., R.G. Gordon, and D.F. Argus, (2010), Geologically current plate motions, *Geophys. J. Int.*, *181*, 1-80, doi: 10.1111/j.1365-246X.2009.04491.x.

DeShon, H. R., S. Y. Schwartz, S. L. Bilek, L. M. Dorman, V. Gonzalez, J. M. Protti, E. R. Flueh, and T. H. Dixon (2003), Seismogenic zone structure of the southern Middle America Trench, Costa Rica, *J. Geophys. Res*., *108*(B10), 2491, doi:10.1029/2002JB002294.

DeShon, H. R., S. Y. Schwartz, A. V. Newman, V. Gonzalez, M. Protti, L. M. Dorman, T. H. Dixon, D. E. Sampson, and E. R. Flueh (2006), Seismogenic zone structure beneath the Nicoya Peninsula, Costa Rica, from three-dimensional local earthquake P- and S-wave tomography, *Geophys. J. Int*., *164*, 109–124, doi:10.1111/j.1365-246X.2005.02809.x.

Dixon, Timothy H; Moore, Casey. The Seismogenic Zone of Subduction Thrust Faults. New York: Columbia University Press, 2012. Ebook Library. Web. 28 Oct. 2014.

Di Toro, G., Goldsby, D.L. & Tullis, T.E., (2004), Friction falls towards zero in quartz rock as slip velocity approaches seismic rates, *Nature*, *427*, 436-439.

Dumitru, T. A. (1991), Effects of subduction parameters on geothermal gradients in forearcs,

with an application to Franciscan subduction in California, *J. Geophys. Res*., *96*, 621–641, doi:10.1029/90JB01913.

Fisher, Andrew T., (1998), Permeability within basaltic oceanic crust., *Reviews of Geophysics*, *36*(2), 143-182, doi: 10.1029/97RG02916.

Fisher, A. T., C. A. Stein, R. N. Harris, K. Wang, E. A. Silver, M. Pfender, M. Hutnak, A. Cherkaoui, R. Bodzin, and H. Villinger (2003), Abrupt thermal transition reveals hydrothermal boundary and role of seamounts within the Cocos Plate, *Geophys. Res. Lett*., *30*(11), 1550, doi:10.1029/2002GL016766.

Fulton, P. M., E. E. Brodsky, Y. Kano, J. Mori, F. Chester, T. Ishikawa, R. N. Harris, W. Lin, N. Eguchi, and S. Toczko, (2013), Low coseismic friction on the Tohoku-Oki fault determined from temperature measurements, *Science*, *342*, 1214-1217.

Gao, X. and K. Wang (2014), Strength of stick-slip and creeping subduction megathrusts from heat flow observations, *Science*, *345*, 1038-1041.

Harris, R. N., and K. Wang (2002), Thermal models of the Middle America Trench at the Nicoya Peninsula, Costa Rica, *Geophys. Res. Lett.*, *29*(21), 2010, doi:10.1029/2002GL015406.

Harris, R. N., I. Grevemeyer, C. R. Ranero, H. Villinger, U. Barckhausen, T. Henke, C. Mueller, and S. Neben (2010), Thermal regime of the Costa Rican convergent margin: 1. Along-strike variations in heat flow from probe measurements and estimated from bottom-simulating reflectors, *Geochem. Geophys. Geosyst*., *11*(12), doi:10.1029/2010GC003272.

Harris, R. N., G. Spinelli, C. R. Ranero, I. Grevemeyer, H. Villinger, and U. Barckhausen (2010), Thermal regime of the Costa Rican convergent margin: 2. Thermal models of the shallow Middle America subduction zone offshore Costa Rica, *Geochem. Geophys. Geosyst*. *11*(12), Q12S29, doi:10.1029/2010GC003273.

Harris, R.N., Sakaguchi, A., Petronotis, K., and the Expedition 344 Scientists, (2013), Proc. IODP, 344: College Station, TX (Integrated Ocean Drilling Program), doi:10.2204/iodp.proc.344.102.2013

Heesemann, M., H. Villinger, A.T. Fisher, A.M. Trehu, and S. Witte, (2007), Testing and deployment of the new APC3 tool to determine insitu temperature while piston coring, in Proc. IODP, Exp. 311, edited by T.S. Collett, M. Riedel, and M.J. Malone, Integrated Ocean Drilling Program, College Station, TX, doi:10.2204/iodp.proc.311.108.

Hutnak, M., and A.T. Fisher (2007), Influence of sedimentation, local and regional hydrothermal circulation, and thermal rebound on measurements of seafloor heat flux, J. Geophys. Res., 112, B12101, doi: 10.1029/2007JB005022.

Hutnak, M., et al. (2007), The thermal state of 18–24 Ma upper lithosphere subducting below the Nicoya Peninsula, northern Costa Rica margin, in *The Seismogenic Zone of Subduction Thrust Faults*, edited by T. Dixon and C. Moore, pp. 86–122, Columbia Univ. Press, New York.

Hutnak, M., A. T. Fisher, R. Harris, C. Stein, K. Wang, G. Spinelli, M. Schindler, H. Villinger, and E. Silver (2008), Surprisingly large heat and fluid fluxes driven through midplate outcrops on ocean crust, *Nat. Geoscience*, *1*, 611–614, doi:10.1038/ngeo264.

Husen, S., R. Quintero, E. Kissling, and B. Hacker (2003), Subduction-zone structure and magmatic processes constrained by local earthquake tomography and petrological modeling, *Geophys. J. Int*., *155*, 11–32, doi:10.1046/ j.1365-236X.2003.01984.x.

Hyndman, R. D., and K. Wang (1993), Thermal constraints on the zone of major thrust earthquake failure: The Cascadia Subduction Zone, *J. Geophys. Res*., *98*(B2), 2039–2060, doi:10.1029/92JB02279.

Hyndman, R. D., M. Yamano, and D. A. Oleskevich, (1997), The seismogenic zone of subduction thrust faults, *Island Arc*, *6*, 244–260.

Ikari, M.J; Niemeijer, A.R., Spiers, K.C., Kopf, A.J.. Saffer, D.M., (2013), Experimental evidence linking slip instability with seafloor lithology and topography at the Costa Rica convergent margin, *Geology*, *41*(8), 891-894, doi:10.1130/G33956.1.

Jeffreys, H. (1938), The disturbance of the temperature gradient in the earth's crust by inequalities of height. Geophysical Journal International, 4: 309–312. doi: 10.1111/j.1365-246X.1938.tb01752.x

Kimura, G., E. A. Silver, and P. Blum, Proceedings ODP, Initial Reports 170, Texas A&M University, College Station, TX, 1997.

Kummer, T., and G. A. Spinelli (2008), Hydrothermal circulation in subducting crust reduces subduction zone temperatures, *Geology*, *36*, 91–94, doi:10.1130/G24128A.1.

Kummer, T., and G. A. Spinelli (2009), Thermal effects of fluid circulation in the basement aquifer of subducting oceanic crust, *J. Geophys. Res*., *114*, B03104, doi:10.1029/2008JB006197.

Kyriakopoulos, C. A.V. Newman, A.M. Thomas, M. Moore-Driskell, and G.T. Farmer (2015), A new seismically constrained subduction interface model for Central America, *J. Geophys. Res.* [in review].

Langseth, M. G., and E. A. Silver (1996), The Nicoya convergent margin—A region of exceptionally low heat flow, *Geophys. Res. Lett*., *23*, 891–894, doi:10.1029/96GL00733.

MacKenzie, L., G. A. Abers, K. M. Fischer, E. M. Syracuse, J. M. Protti, and W. Strauch (2008),

Crustal structure along the southern Central American volcanic front, *Geochem. Geophys. Geosyst*., *9*, Q08S09, doi:10.1029/2008GC001991.

Marone, C., and C. H. Scholz (1988), The depth of seismic faulting and the upper transition from stable to unstable slip regimes. *Geophys. Res. Lett*., *15*, 621 – 624.

Molnar, P., and P. England (1990), Temperatures, heat flux, and frictional stress near major thrust faults, *J. Geophys. Res*., *95*(B4), 4833–4856, doi:10.1029/JB095iB04p04833.

Moore, J. C., and D. Saffer (2001), Updip limit of the seismogenic zone beneath the accretionary prism of southwest Japan: An effect of diagenetic to low-grade metamorphic processes and increasing effective stress, Geol., 29(2), 183 – 186.

Newman, et al. (2002), Along-strike variability in the seismogenic zone below Nicoya Peninsula, Costa Rica, *Geophys. Res. Lett.*, *29*(20), 1977, doi:10.1029/2002GL015409.

Oleskevich, D. A., R. D. Hyndman, and K. Wang (1999), The updip and downdip limits to great subduction earthquakes: Thermal and structural models of Cascadia, south Alaska, SW Japan, and Chile, *J. Geophys. Res*., *104*, 14,965–14,991, doi:10.1029/1999JB900060.

Peacock, S. M., and K. Wang (1999), Seismic consequences of warm versus cool subduction metamorphism: Examples from southwest and northeast Japan, *Science*, *286*, 937–939.

Powell, W.G., D.S. Chapman, N. Balling, A.E. Beck, (1988), Continental Heat-Flow Density, in *Handbook of Terrestrial Heat-Flow Density Determination, Solid Earth Sciences Library*, vol. 4, pp 167-222.

Protti, M., F. Güendel, and K. McNally (1994), The geometry of the Wadati-Benioff zone under southern Central America and its tectonic significance: Results from a high-resolution local seismographic network, *Phys. Earth Planet. Inter*., *84*, 271–287, doi:10.1016/0031-9201(94) 90046-9.

Protti, M., et al. (1995), The March 25, 1990(Mw = 7.0, ML = 6.8), earthquake at the entrance of the Nicoya Gulf, Costa Rica: Its prior activity, foreshocks, aftershocks, and triggered seismicity, J. Geophys. Res., 100(B10), 20,345– 20,358, doi:10.1029/94JB03099.

Ranero, C. R., A. Villaenor, J. Phipps Morgan, and W. Weinrebe (2005), Relationship between bend-faulting at trenches and intermediate-depth seismicity, *Geochem. Geophys. Geosyst*., *6*, Q12002, doi:10.1029/2005GC000997.

Ranero, C. R.; Grevemeyer, I.; Sahling, H.; Barckhausen, U.; Hensen, C.; Wallmann, K.; Weinrebe, W.; Vannucchi, P.; von Huene, R.; McIntosh, K. (2008). Hydrogeological system of erosional convergent margins and its influence on tectonics and interplate seismogenesis. *Geochem. Geophys. Geosyst*., *9*, Q03S04, doi:10.1029/2007GC001679

Ratcliffe, E.H., (1960), The thermal conductivities of ocean sediments. *J. Geophys. Res*., *65*(5), 1535-1541, doi:10.1029/JZ065i005p01535.

Saffer, D.M., and C. Marone, (2003), Comparison of smectite-and illite-rich gouge frictional properties: application to the updip limit of the seismogenic zone along subduction megathrusts, *Earth Planet. Sci. Lett*., *215*, 219-235.

Schwartz, S. Y., and H. R. DeShon (2007), Distinct updip limits to geogetic locking and microseismicity at the northern Costa Rica seismogenic zone: Evidence for two mechanical transitions, in The Seismogenic Zone of Subduction Thrust Faults, edited by T. Dixon and C. Moore, pp. 576–599, Columbia Univ. Press, New York.

Spinelli, G. A., and D. M. Saffer (2004), Along-strike variations in underthrust sediment dewatering on the Nicoya margin, Costa Rica related to the updip limit of seismicity, *Geophys. Res. Lett*., *31*, L04613, doi:10.1029/2003GL018863.

Spinelli, G. A., and K. Wang (2008), Effects of fluid circulation in subducting crust on Nankai margin seismogenic zone temperatures, *Geology*, *36*, 887–890, doi:10.1130/G25145A.1.

Spinelli, G. A., and K. Wang (2009), Links between fluid circulation, temperature, and metamorphism in subducting slabs, *Geophys. Res. Lett*., *36*, L13302, doi:10.1029/2009GL038706.

Spinelli, G. A. and Underwood, M. B. (2004), Character of sediments entering the Costa Rica subduction zone: Implications for partitioning of water along the plate interface, *Island Arc*, *13*, 432–451, doi: 10.1111/j.1440-1738.2004.00436.x.

Stein, C., and S. Stein (1992), A model for the global variation in oceanic depth and heat flow with lithospheric age, *Nature*, *359*, 123–129, doi:10.1038/359123a0.

Turcotte, D.L. & G. Schubert (1982), *Geodynamics: Applications of Continuum Physics to Geological Problems*, John Wiley & Sons, New York.

Valentine, R., J. D. Morris, and D. Duncan, (2000), Sediment subduction, accretion, underplating and erosion along the Costa Rica margin: Constraints from 10Be, Geol. Soc. Amer. Bull.

Vacquier, V., J. G. Sclater, and C. E. Correy, (1967), Studies of the thermal state of the Earth: Heat flow, Eastern Pacific, Bull, Earthquake Res. Inst., 45, 375– 393.

Vacquier, V., (1985), The measurement of thermal conductivity of solids with a transient linear heat source on the plane surface of a poorly conducting body. *Earth Planet. Sci. Lett*., *74* (2-3):275–279. doi:10.1016/0012-821X(85)90027-5

Vannucchi, P., D. W. Scholl, M. Meschede, and K. McDougall-Reid (2001), Tectonic erosion and consequent collapse of the Pacific margin of Costa Rica: Combined implications from ODP Leg 170, seismic offshore data, and regional geology of the Nicoya Peninsula, *Tectonics*, *20*(5), 649–668, doi:10.1029/2000TC001223.

Vannucchi, P., C. R. Ranero, S. Galeotti, S. M. Straub, D. W. Scholl, and K. McDougall-Ried (2003), Fast rates of subduction erosion along the Costa Rica Pacific margin: Implications for nonsteady rates of crustal recycling at subduction zones, *J. Geophys. Res*., *108*, 2511, doi:10.1029/2002JB002207, B11.

Vannucchi, P., Ujiie, K., Stroncik, N., Malinverno, A., and the Expedition 334 Scientists, (2012), Proc. IODP, 334: Tokyo (Integrated Ocean Drilling Program Management International, Inc.). doi:10.2204/iodp.proc.334.101.2012

Vannucchi, P., Sak, P.B., Morgan, J.P., Ohkushi, K., Ujiie, K., and the Expedition 334 Scientists (2013), Rapid pulses of uplift, subsidence, and subduction erosion offshore Central America: Implications for building the rock record of convergent margins, *Geology*, *41*, 995- 998, doi:10.1130/G34355.1

Vacquier, V., (1985), The measurement of thermal conductivity of solids with a transient linear heat source on the plane surface of a poorly conducting body. *Earth Planet. Sci. Lett*., *74*(2–3):275–279. doi:10.1016/0012-821X(85)90027-5

Von Herzen, R., and Maxwell, A.E., (1959), The measurement of thermal conductivity of deep-sea sediments by a needle-probe method. *J. Geophys. Res*., *64*(10), 1557-1563., doi:10.1029/JZ064i010p01557

von Huene, R., and D. W. Scholl (1991), Observations at convergent margins concerning sediment subduction, subduction erosion, and the growth of continental crust, *Rev. Geophys*., *29*(3), 279–316, doi:10.1029/91RG00969.

Walther, C.H.E., (2003), The crustal structure of the Cocos Ridge off Costa Rica. *J. Geophys. Res.: Solid Earth*, *108*(B3):2136. doi:10.1029/2001JB000888.

Wang, K., T. Mulder, G. C. Rogers, and R. D. Hyndman (1995), Case for very low coupling stress on the Cascadia subduction fault, *J. Geophys. Res*., *100*, 12,907–12,918, doi:10.1029/95JB00516.

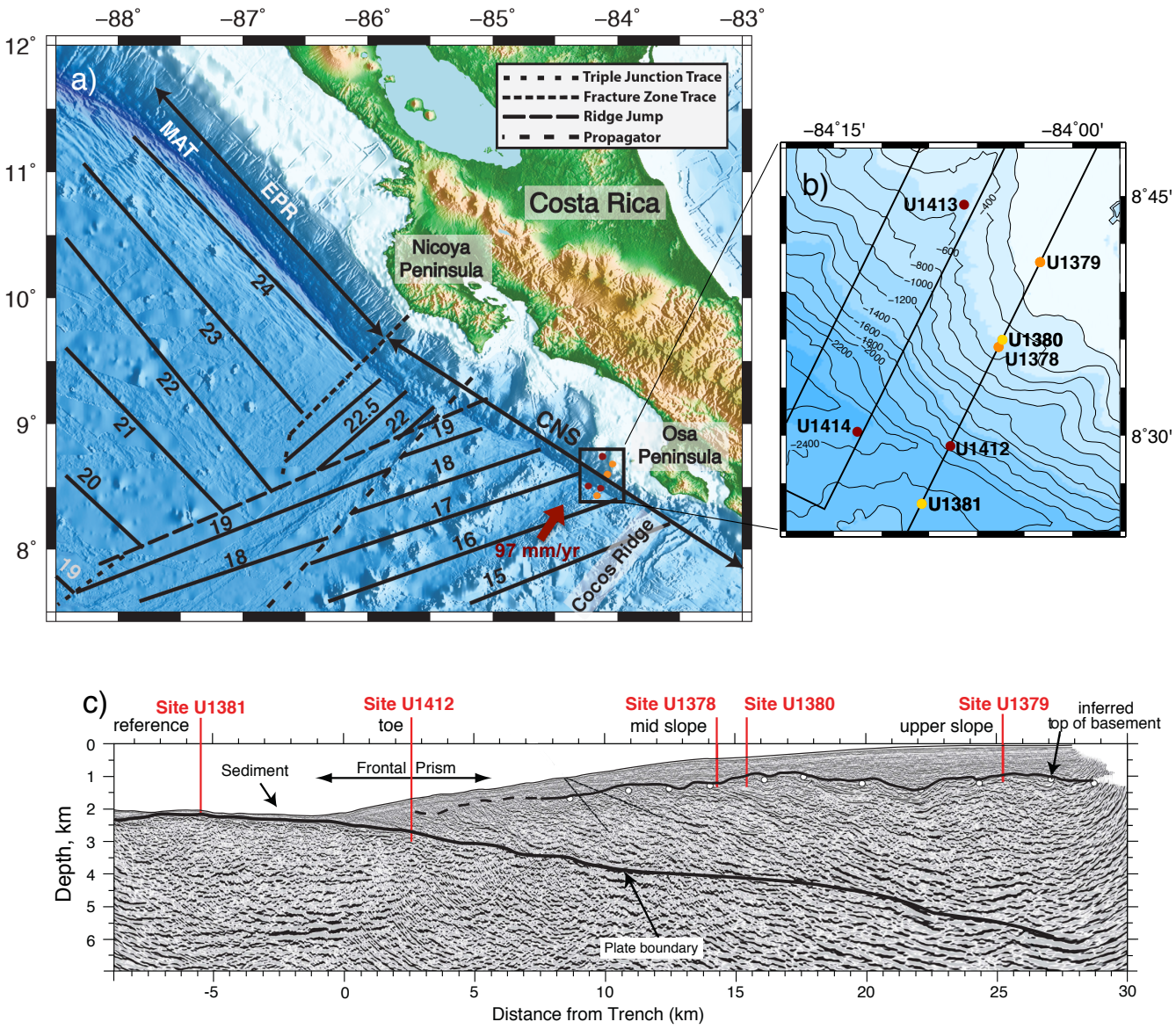

Figure 1. a) Map showing major tectonic features of the Costa Rica Margin [modified from *Barckhausen et al.*, 2001]. Crust north of the plate suture was generated at the fast-spreading East Pacific Rise (EPR); crust south of the plate suture was generated at the intermediate-spreading Cocos-Nazca Spreading Center (CNS). Age isochrons (My), are marked as solid black lines. The plate convergence vector at the location of the CRISP study area is ~97 mm/yr. b) Bathymetric map of IODP drill sites from Expeditions 334 and 344. The solid black line shows the CRISP transect along which heat flow analysis is conducted. c) Seismic section BGR-99 Line 7 showing locations of CRISP sites with inferred plate boundary and upper plate basement.

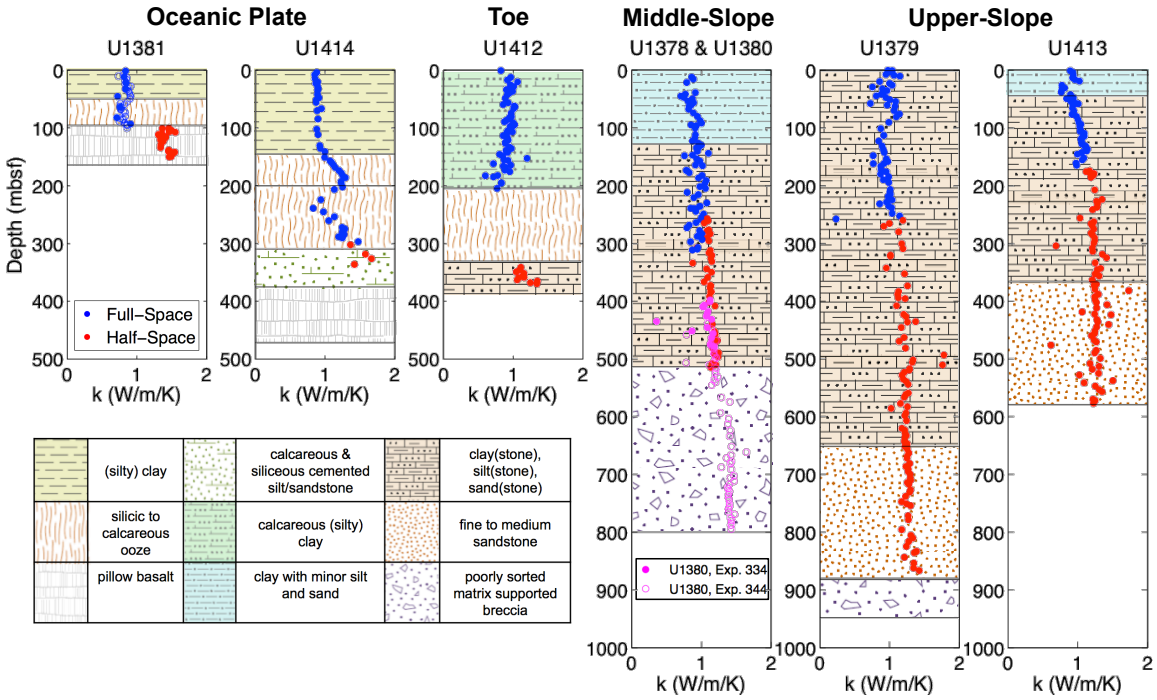

Figure 2. Thermal conductivity, k, as a function of depth and lithology. Measurements for sites U1378 and U1380 are located within 1 km of each other and are grouped together for this study. All measurements at site U1380 were made with the half-space technique, as described in the text.

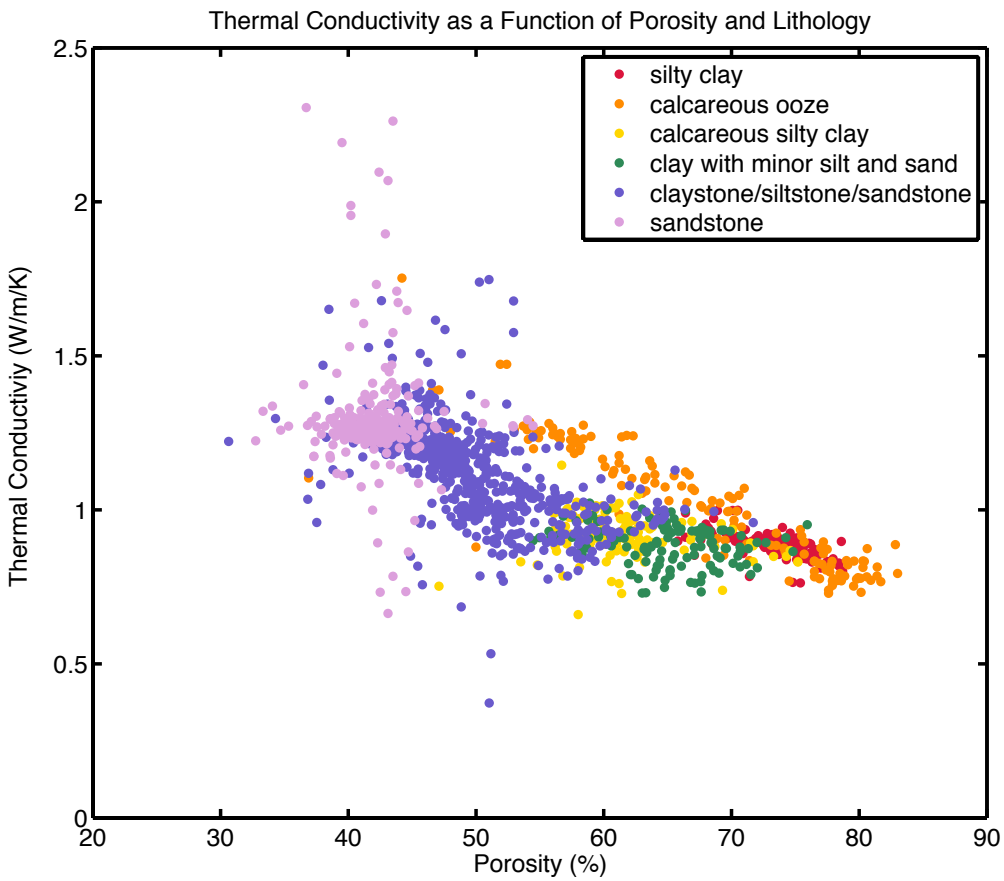

Figure 3. Thermal conductivity as a function of porosity and major lithologic units.

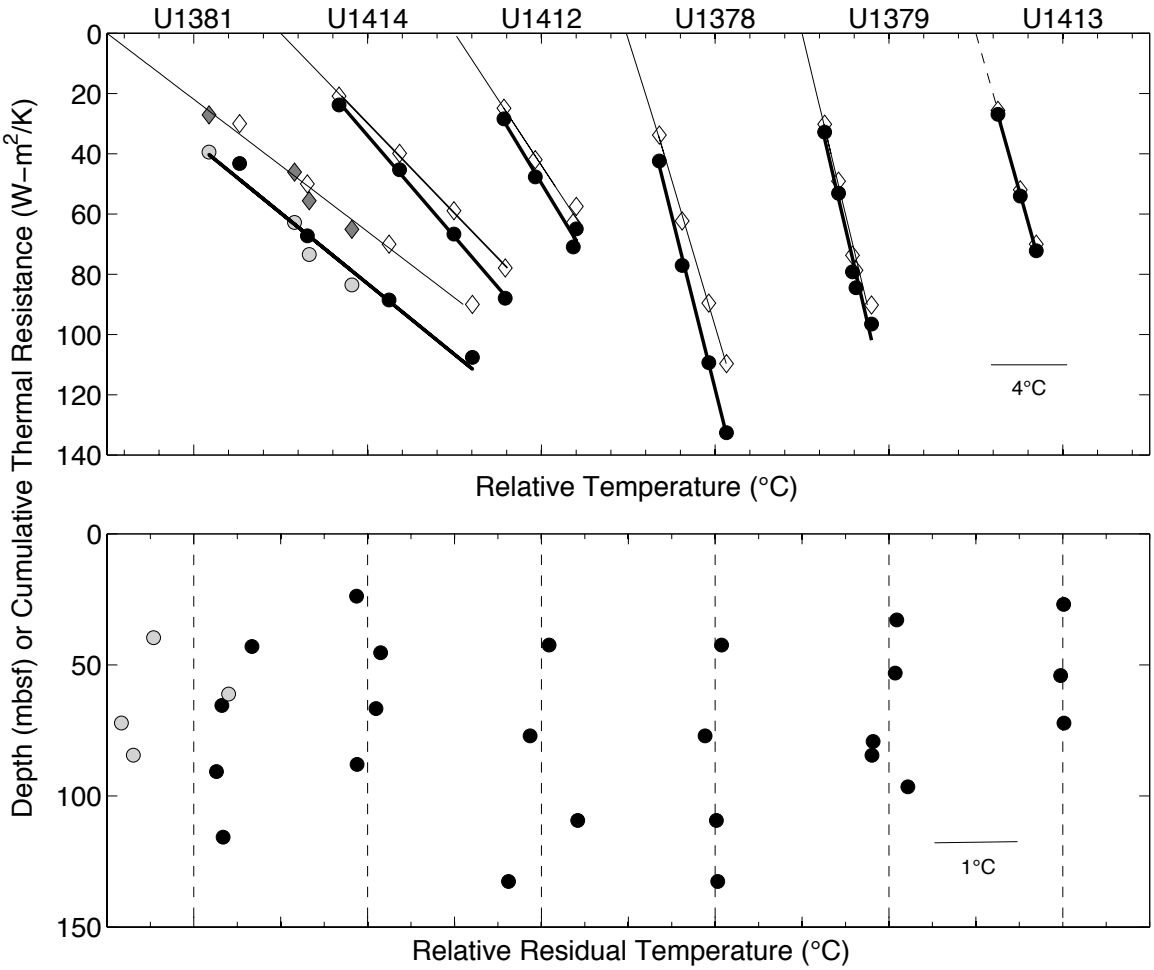

Figure 4. a) Temperature versus depth (open diamonds) and cumulative thermal resistance (solid symbols) used to determine heat flow values. Note that a relative temperature scale is used to avoid overlap. Temperatures measurements for site U1381 on Expedition 344 are shaded in gray. b) Temperature residuals between observed temperature values and best-fit values to temperature versus thermal resistance lines. Residual temperatures are offset to avoid overlap. Estimates of standard deviation are reported in Table 1.

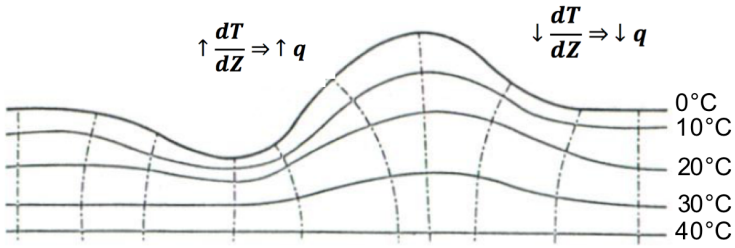

Figure 5. Schematic illustration showing effect of uneven seafloor bathymetry on subsurface isotherms for a theoretical surface. Modified from *Powell et al.* [1988]. Measured heat flow will be higher than the heat flow at depth if measured in valleys, and lower than heat flow at depth if measured on ridges or local highs.

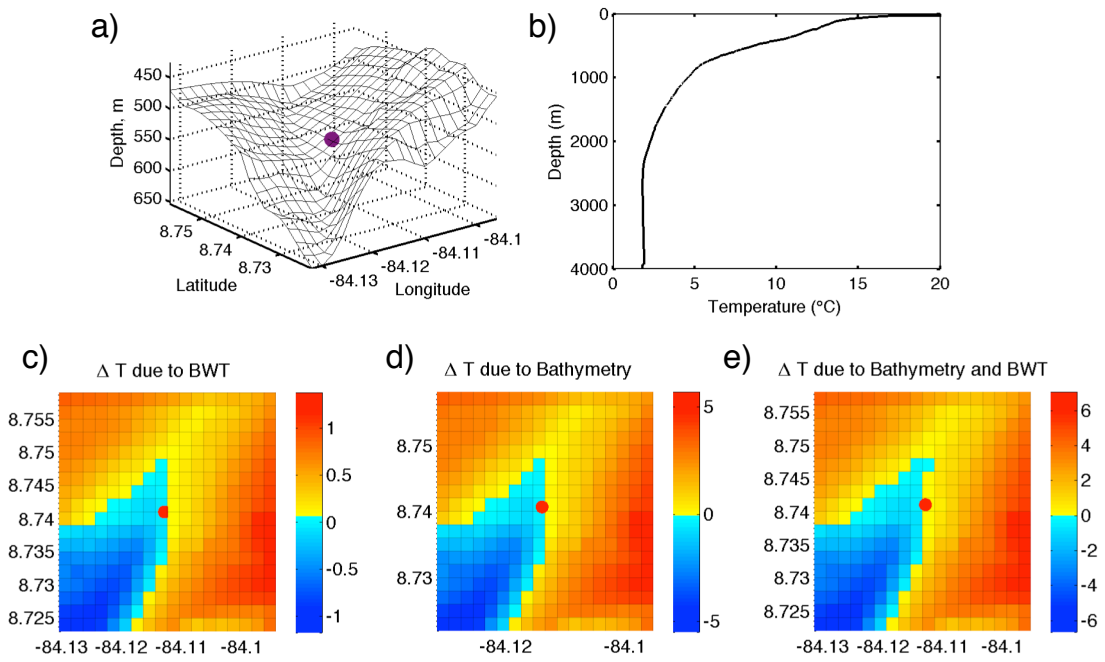

Figure 6. Example bathymetric correction calculations for site U1413.a) 2 km x 2 km bathymetry grid surrounding site U1413 showing its position in a local valley, b) temperature-depth profile from nearby CTD casts, c) difference in grid temperatures between uneven surface and plane at seafloor elevation of core site. d) difference in grid temperatures between surface and borehole plane resulting from observed subsurface gradient. e) Sum of temperature differences due to bottom water temperature and bathymetry.

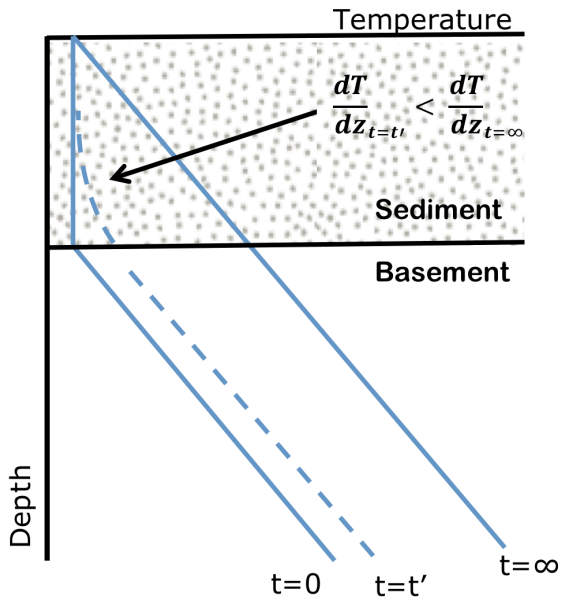

Figure 7. Schematic illustration showing the effect of rapid sedimentation at time t=0 on the near-surface temperature gradient. The transient effect on the surface gradient is shown with the dotted line at t=t' and the final equilibrium state is shown at time t=∞. Measurements of the temperature gradient (and heat flow) made before the sediment layer has equilibrated with the background gradient will be lower than the actual gradient at depth.

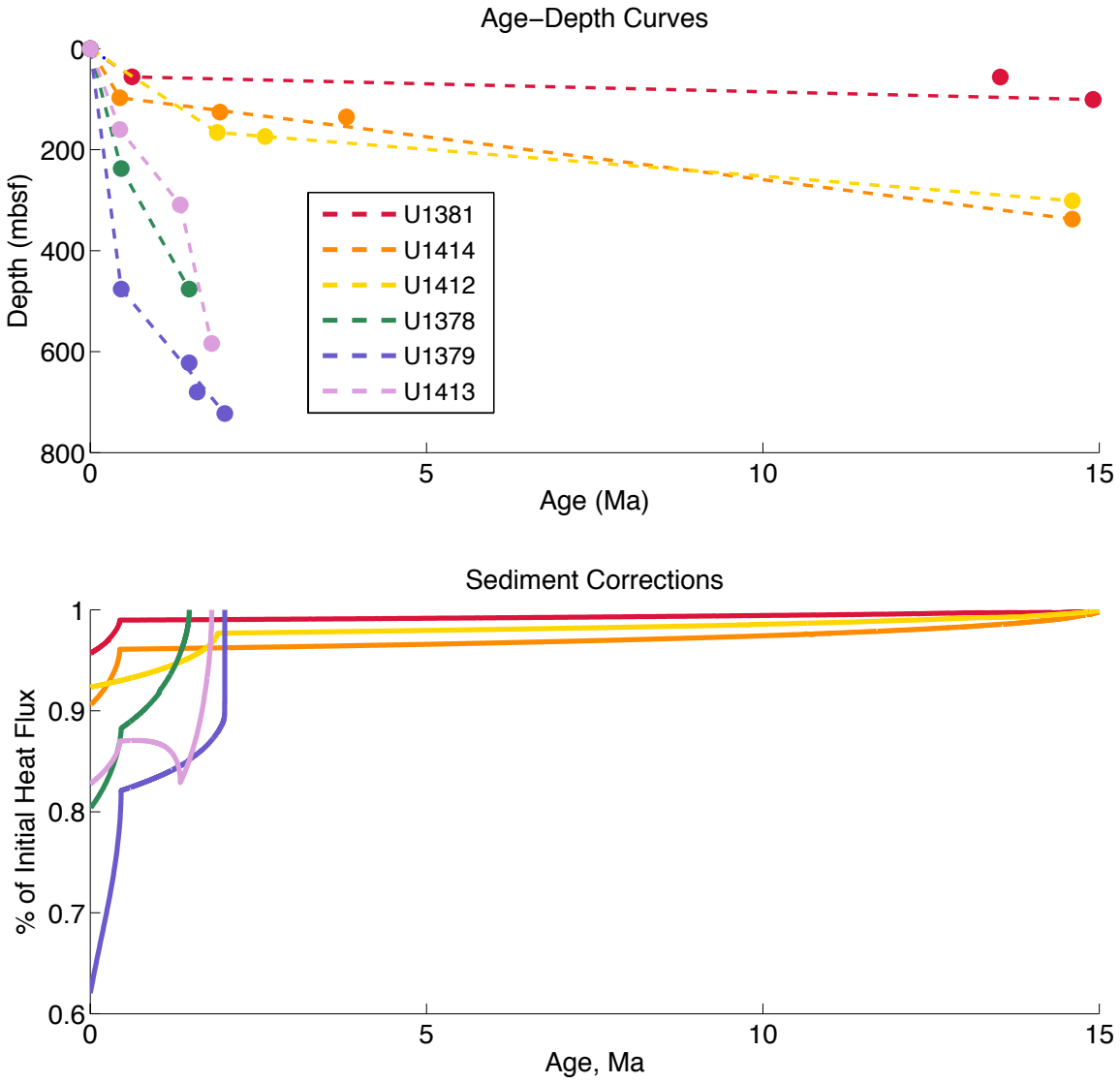

Figure 8. Summary of sedimentation corrections. a) Sediment age-depth plots for all sites, based off calcareous nanofossil ages reported in Table 2b. b) Modeled sedimentation correction as a percent of original heat flow [Hutnak and Fisher, 2007].

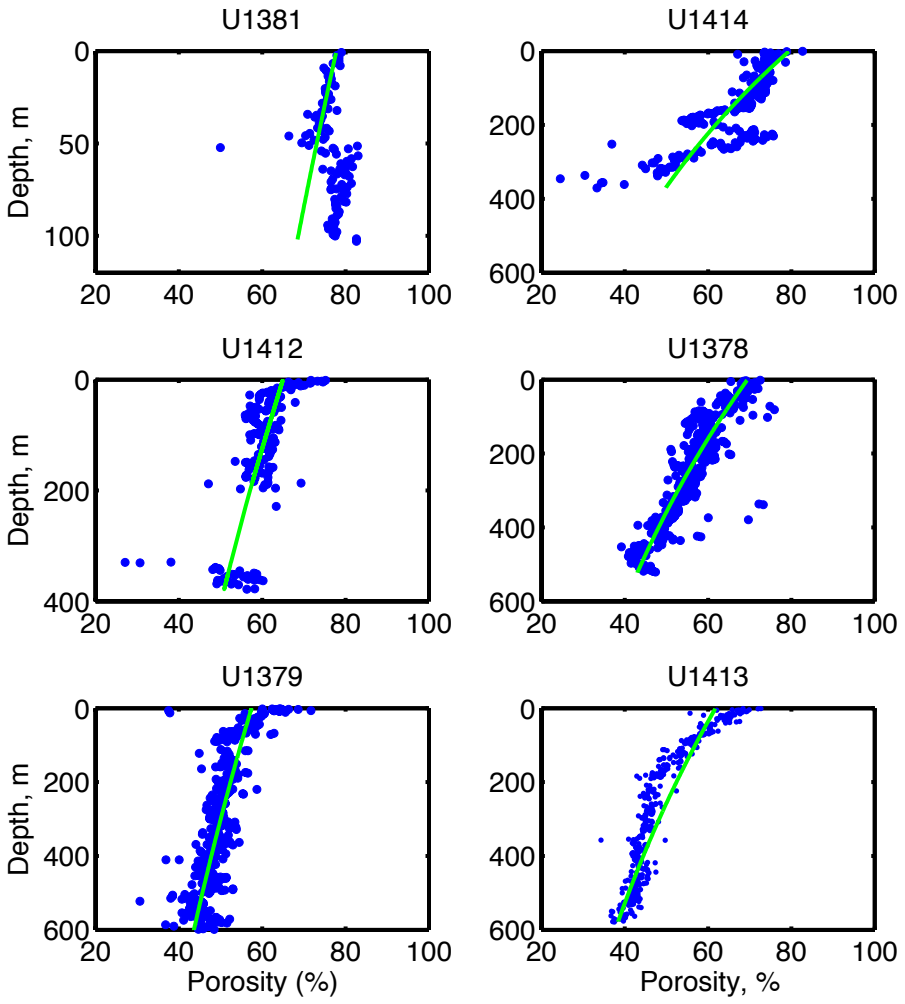

Figure 9. Porosity as a function of depth at each site with best-fit Athy's law curves (green lines). Best fitting parameters for Athy's law are reported in Table 2.

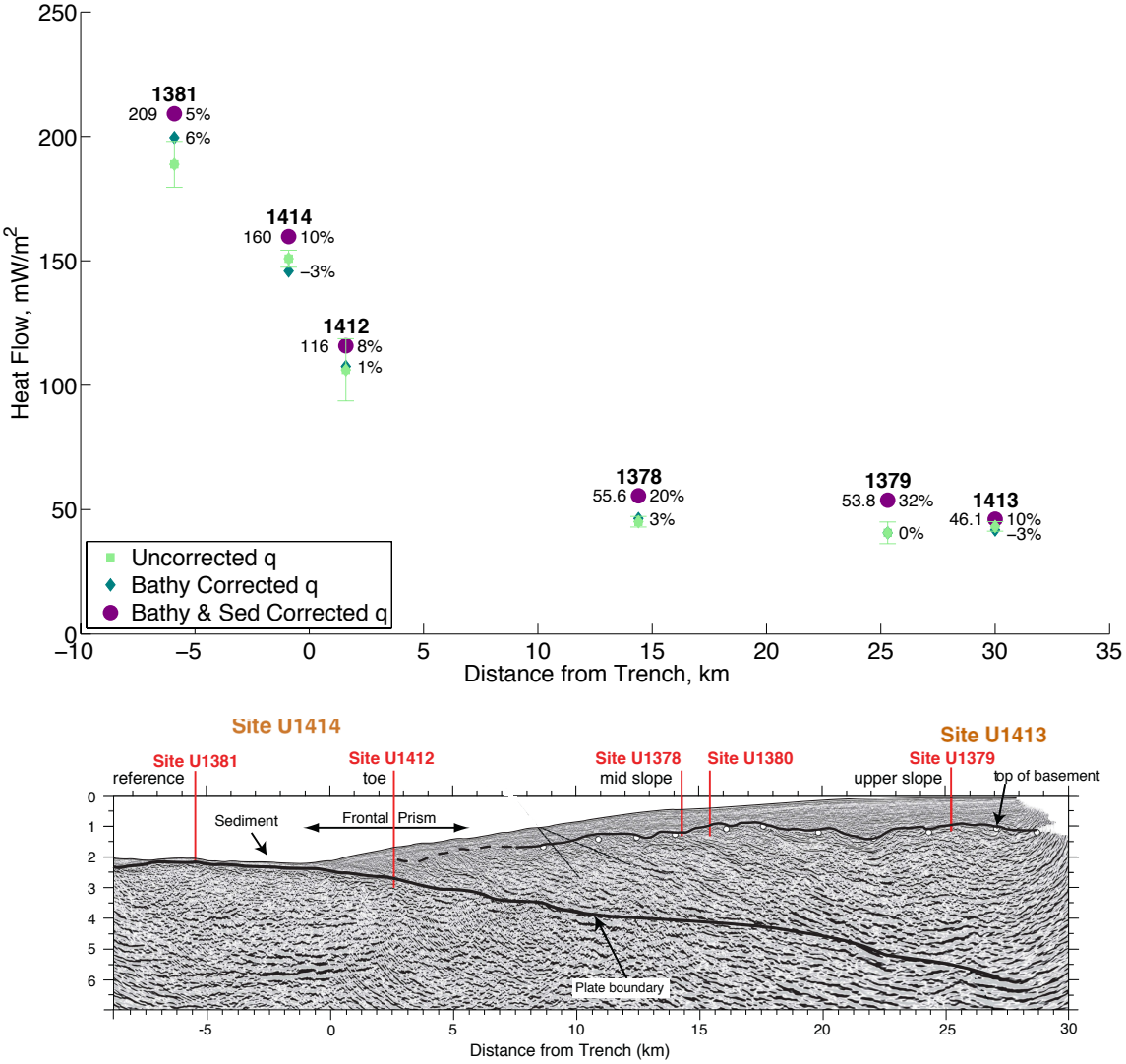

Figure 10: Summary of bathymetric and sedimentation corrections for borehole heat flow values.

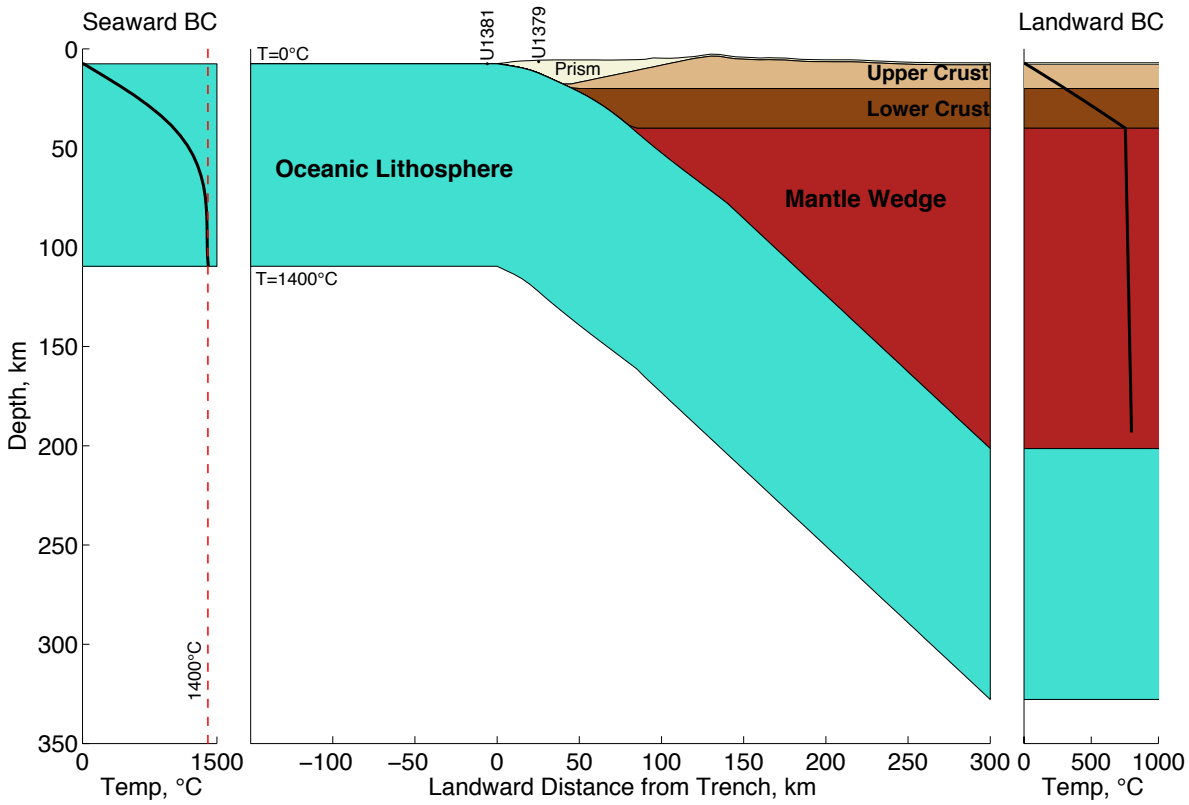

Figure 11: Thermophysical model units and boundary conditions (BCs) for thermal model of subduction. *Left*: Seaward temperature boundary condition is set by the half-space cooling model for 16Ma crust with 100m of sediment cover. *Middle*: Model consists of a 100km thick oceanic lithosphere, a sedimentary prism, upper and lower crust, and a mantle wedge. *Right*: Landward temperature boundary condition consists of 70 mW/m^2 geotherm through the upper plate crust (corresponding to a temperature gradient of 24°C/km for uniform thermal conductivity of 2.9 mW/m^2) and an adiabatic mantle gradient of 0.3°C/km. The landward condition is set sufficiently far from the region of interest (within 50km of the trench) to avoid boundary effects.

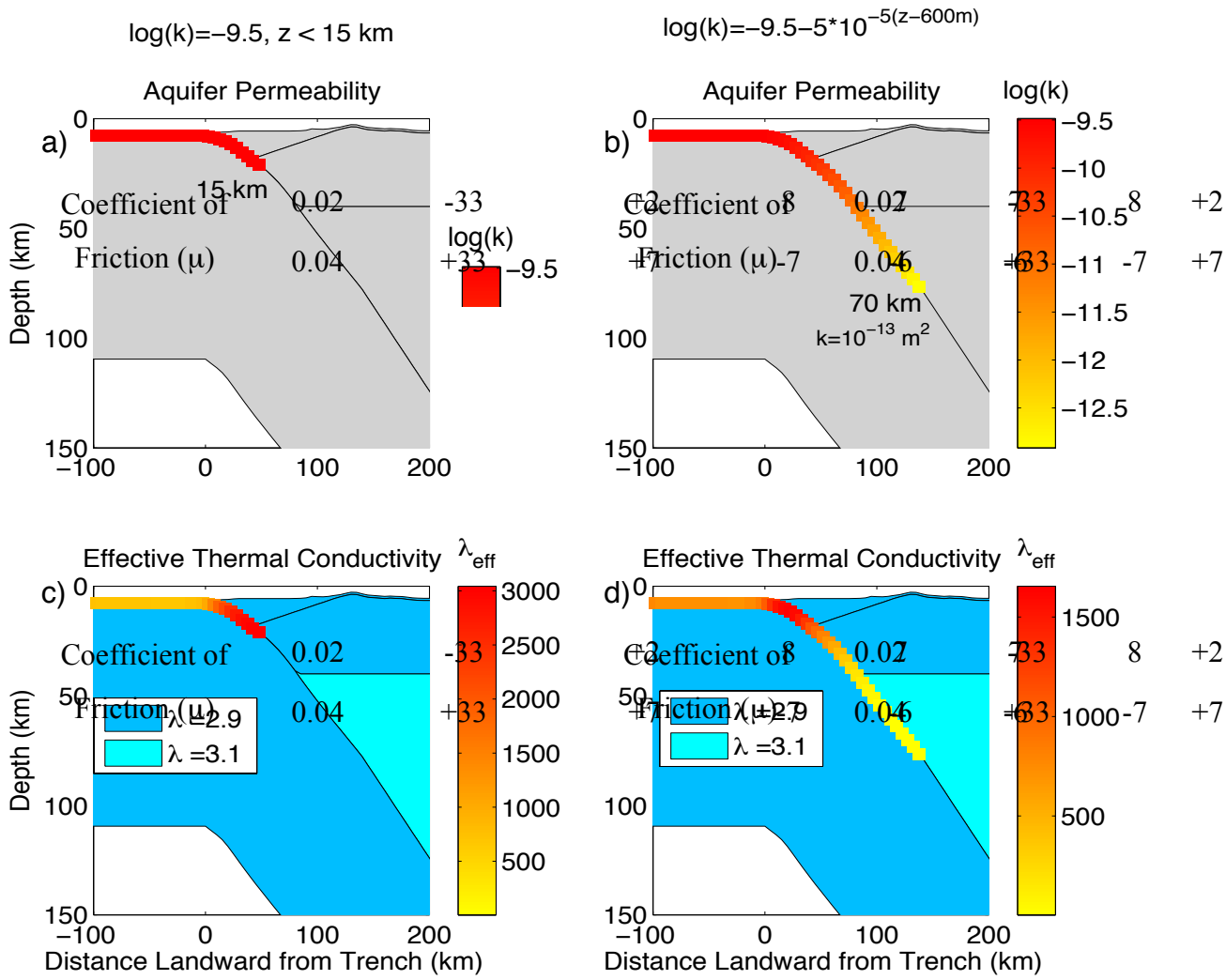

Figure 12. Comparison of oceanic aquifer permeability structures tested, and resulting effective thermal conductivities calculated from the Nusselt number technique. a) and b) Aquifer permeabilities, in m^2, where the inferred deepest extent of hydrothermal circulation is labeled in km below sea floor. Panel a) shows the case for constant aquifer permeability of $10^{-9.5}$ m^2 to a cutoff depth of 15 km. Panel b) shows aquifer permeability that exponentially decreases according to the function $\log(k) = -9.5 - 5*10^{-5(z-600m)}$. The depth at which the aquifer becomes advectively impermeable, at values of $k <= 10^{-13}$ m^2 is 70 km. Panels c) and d) show the calculated effective thermal conductivies, λ_{eff} of the 600 m thick aquifer (not to scale), in W/m/K, for permeability structures shown in a) and b), respectively. The conductivity of the subducting oceanic plate and mantle wedge remain fixed at 2.9 and 3.1 W/m/K.

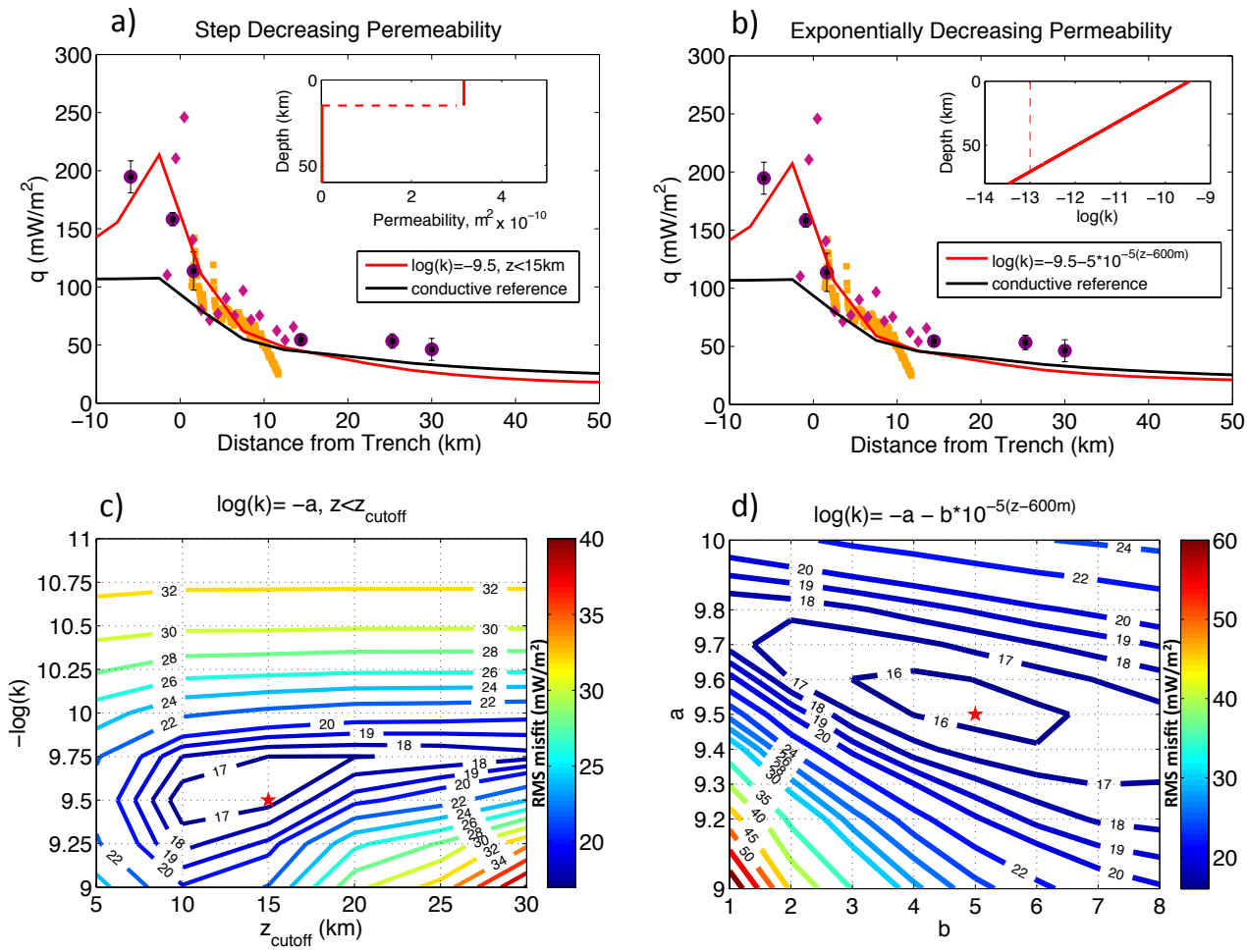

Figure 13. Thermal model results for two sets of permeability structures along the CRISP drilling transect. a) and b) Surface heat flow showing IODP values (purple circles), along with values estimated from shallow probe (small diamonds), and depth to BSRs (orange circles), as reported by *Harris et al.*, 2010b. The black line shows model results where there is no hydrothermal circulation within the uppermost basement, and red line show model results including circulation within the 600 m thick basement aquifer. Panel a) shows fluid flow case for constant permeability, k, within the aquifer to cutoff depth (z_{cutoff}). Panel b) shows model results for fluid flow within the 600 m thick basement aquifer, where permeability is specified by an exponentially decreasing function of the form $\log(k) = -a - b*10^{-5(z-600m)}$. Insets shows preferred permeability model. Panels c) and d) show the RMS misfit between the observed and modeled surface heat flow for models with variable parameters for each permeability structure.

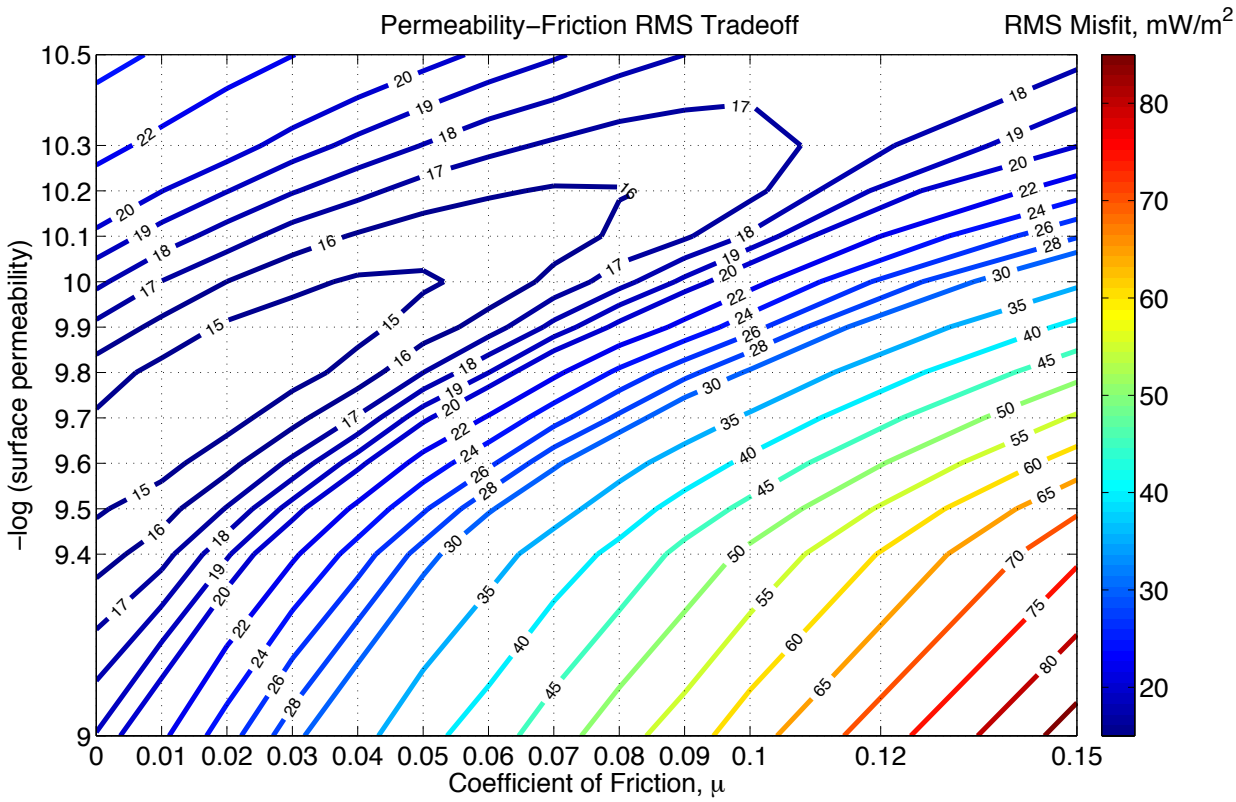

Figure 14: Contour plot of root-mean-square misfit between modeled and observed coefficient of friction for variable aquifer surface permeability and coefficient of friction. Models incorporate hydrothermal circulation within a 600 m thick basement aquifer whose permeability decreases exponentially with depth according to the function $\log(k) = -k_0 - 5*10^{-5(z-600m)}$.

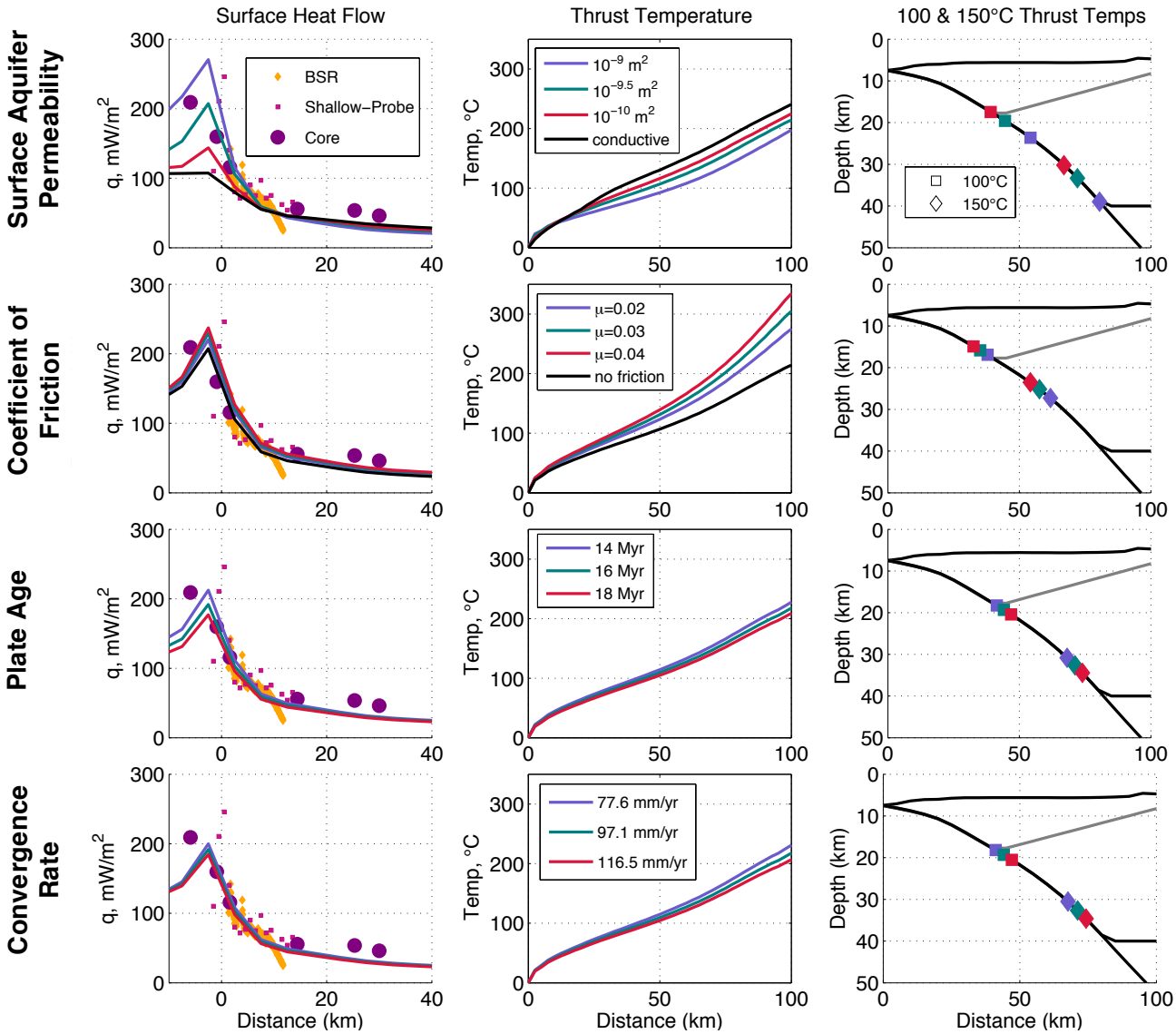

Figure 15: Sensitivity tests of modeled surface heat flow (left), thrust temperature (center), and position of 100° C and 150° C isotherms along the thrust (right) for varying aquifer permeability (a-c), coefficient of friction (d-f), plate age (g-h), and convergence rate (i-k). Models incorporate hydrothermal circulation within a 600 m thick basement aquifer whose permeability decreases exponentially with depth according to the function $\log(k) = -9.5 - 5*10^{-5(z-600m)}$.

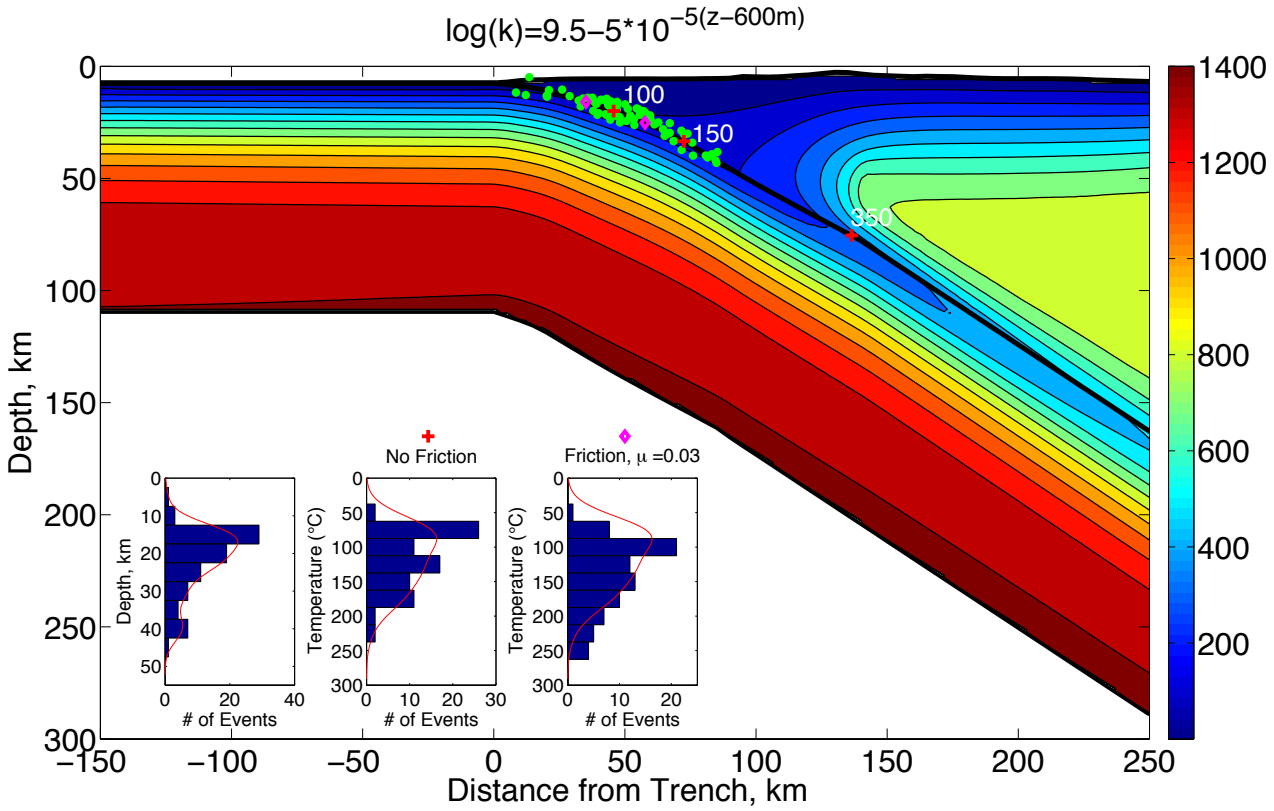

Figure 16: a) Preferred thermal model subduction zone temperatures correlation with interplate seismicity. Thermal contours lines have 100° C spacing and the intersection of the 100, 150, and 350°C isotherms with the subduction thrust are plotted as red crosses for the model including friction and as magenta diamonds for the model without friction. Green dots are relocated hypocenters of seismic events captured following the 1999 M_w 6.9 Quepos earthquake and 2002 M_w 6.4 Osa earthquake. Insets show the distribution of events along the thrust as a function of depth (left), the distribution of event temperatures associated with events according to the nonfrictional model (middle), and temperatures associated with events according to model including friction (right).

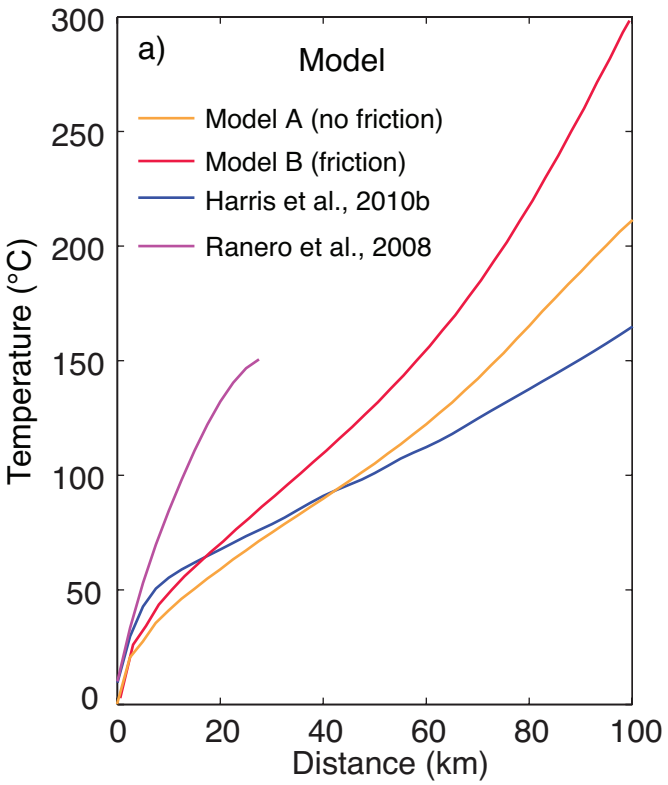

Figure 17. Thrust temperatures of the preferred models, compared to models by *Ranero et al.* [2008] and *Harris et al.* [2010b]. Models A and B incorporate hydrothermal circulation within a 600m thick basement aquifer where permeability decreases exponentially with depth according to the function $\log(k)=9.5-5*10^{-5(z-600m)}$. Model A does not include frictional heating, and Model B incorporates frictional heating where the coefficient of friction along the plate boundary is 0.03.

Table 1. Summary table of heat flow calculations.

Site	Expedition	Latitude (deg min)	Longitude (deg min)	$k \pm \sigma_k$ $Wm^{-1}K^{-1}$	Number of temperature measurements (mbsf)	Depth range of temperature measurements (mbsf)	$q \pm \sigma_q$ (mWm^{-2})	BWT (°C)	Seafloor depth (m)
U1381	334 344 both	8 25.7	-84 9.48	0.83 ± 0.05 0.80 ± 0.07 0.83 ± 0.05	4 4 8	30-90 27.1-65.1 27.1-90	185 ± 3 179 ± 20 189 ± 9	1.6 1.2 0.9	2069.1
U1414	344	8 30.23	-84 13.53	0.89 ± 0.02	4	20.9-77.9	151 ± 3	2.4	2458.6
U1412	344	8 29.17	-84 7.75	0.91± 0.09	4	24.9-62.9	106 ± 13	2.4	1920.7
U1378/ U1380	334 334/344	8 35.54 8 36.00	-84 4.63 -84 4.40	8.42e-4(z)+0.787 σ=0.0824	4	33.8-109.7	45±2	7.8	525.4
U1379	334	8 40.86	-84 2.03	5.25e-4(z)+0.911 σ=0.1332	5	30.2-90.2	41 ± 4	14.4	127.7
U1413	344	8 44.45	-84 6.80	8.32e-4(z)+0.941 σ=0.1906	3	25.6-70	43 ± 2	7.8	540.4

k is thermal conductivity and σ_k is standard deviation. Values are reported as means if no trend is observed or as a linear fit as a function of depth where there is a trend. q is the heat flow calculated according to Bullard's method, as described in the text. BWT is the bottom water temperature, determined from the surface temperature intercept.

Table 2. Sediment accumulation data and porosity values used in sedimentation corrections.

Site	Age Range (Ma)	Duration (Myr)	Accumlation Rate (m/Myr)	Drilled Sediment Thickness (m)	ϕ_o	L (m)
U1413	0-0.44	0.44	364	579	0.62	1214
	0.44-1.34	0.902	166			
	1.34-1.81	0.4652	590			
U1379	0-0.46	0.46	1035	882	0.57	2179
	0.46-2	1.5393	160			
U1378	0-0.46	0.46	516	514	0.70	1091
	0.46-1.47	1.0135	236			
U1412	0-1.89	1.89	90	331	0.65	1546
	1.89-15	12.21	11			
U1414	0-0.44	0.44	221	375	0.80	793
	0.44-14.6	14.6	17			
U1381	0-0.44	0.44	90	95	0.78	799
	*hiatus					
	0.44-15	14.6	4			

ϕ_o and L are the surface porosity and decay parameter used in Athy's Law (Equation 6).

Table 3. Model parameters used in sedimentation correction models.

Model Parameter	Value
Thermal Conductivity (W/m/K)	
Water	0.6
Sediment Grain	1.7
Basement	2.7
Thermal Capacity (J/m^3 K)	
Water	4.30e6
Sediment Grain	2.65e6
Basement	3.10e6

Table 4. Heat Flow Correction Summary.

Site	Bathymetry Correction %	Sedimentation Correction %	Corrected Heat Flow (mW/m^2)
U1413	-3.3	+10	46
U1379	N/A*	+32	53
U1378	+3	+20	54
U1412	+1	+8	114
U1414	-3	+10	158
U1381	+6	+5	195

*Bathymetric correction could not be applied to site U1379 due to lack of sufficient bathymetry data coverage in this area.

Table 5. Thermal model parameters.

Unit	Thermal Conductivity W/m-K	Heat Capacity MJ/m^3-K	Heat Production $\mu W/m^3$
Choretoga Block (0-40 km)	2.9	--	0.2
Prism	2.9	--	0.2
Sediments (100 m)	0.9	2.6	0.2
Oceanic Plate	2.9	3.3	0.3
Mantle Wedge	3.1	3.3	0.2

Table 6. Sensitivity of position of isotherms along the subduction thrust due to selected model parameters.

Parameter	Value	Parameter Perturbation (%)	Change in RMS misfit (mW/m^2)	Percent change to position of isotherms along the subduction thrust			
				100° C		150° C	
				x (km)	z (km)	x (km)	z (km)
Age (Ma)	14	-12	+0.2	-6	-6	-4	-6
	18	+12	+2	6	6	4	5
Convergence Rate (mm/yr)	77.6	-20	-0.2	-7	-6	-5	-7
	116.5	+20	+1	7	6	4	6
Coefficient of Friction (μ)	0.02	-33	+2	8	7	7	8
	0.04	+33	+7	-7	-6	-6	-7

Parameter perturbations and associated percent changes in isotherm positions are in reference to a model with a 16 Ma crust and convergence rate of 97.1 mm/yr, which has an RMS misfit to the observed heat flow data of 16 mW/m^2. Sensitivity tests for the coefficient of friction are in reference to a model with μ=0.03, all other tests are conducted relative to a model with no frictional heating. Negative changes in isotherm positions indicate an updip shift.